ROYAL INSTITUTE
OF TECHNOLOGY

Nonlinear carbon structures for mode-locking of fiber lasers

PAVEL DELGADO-GOROUN

Master of Science Thesis at
The Royal Institute of Technology
Department of Laser Physics
Supervisor: Valdas Pasiskevicius
Examiner: Lars-Gunnar Andersson

TRITA-FYS 2014:52

Abstract

Both solid-state and fiber lasers have successfully been passive mode-locked using carbon structures, such as carbon nanotubes (CNT) and graphene as saturable absorbers (SA). In order to get the correct amount of SA onto the substrate a trial and error approach is used today. The main goal of this project is therefore the creation of an optical setup for characterizing an all fiber module and measuring the nonlinear response of the sample. By using a probe laser of 100 mW at 1046 nm, with 160 fs pulse duration, the transmission data of the substrate was acquired.

The SA material used in this thesis were CNTs, with concentrations of 0.1 mg/ml dispersed in 1.2-dichlorobenzene (DCB), which were centrifuged to separate any ash-residuals from the CNTs and allow easy extraction of the top layer with the CNTs.

The first objective was to fabricate a SA fiber sample. Two fiber types were investigated in this thesis, a two holed fibers and a commercial single mode fiber. Using pressure in order to fill the fiber with a solution of CNTs and measure the evanescent field interaction, the preliminary study did not give any conclusive results. Instead a CNT attachment process on the single mode fiber-end was conducted in order to deposit CNTs on the fiber-end surface for a direct interaction between the CNTs and the guided light. The attached CNTs where confirmed both visually with a microscope and an optical spectrum analyzer (OSA), where the change of lower transmission was observed with more attached CNTs.

The second objective was to create the characterization setup which was developed, to work using two set of measurements, one of a reference fiber and second of the substrate, in order to obtain their transmission data for comparison. The transmission measurement was performed by measuring a fraction of the laser output and the guided light output from the fiber using a single diode. The dynamic range reached 44 dB with this method and some nonlinear effects where measurable at 2000 μJ/cm^2. The high fluence required was most probable due to the CNTs got deposited around the core where only evanescent field interaction occurred, therefore also never completely saturating the SA. A higher laser output is therefore required in order to get hold of the saturation fluence, non-saturable loss and the saturation depth for this case.

But the CNTs where also expected to detach themselves over time since the CNTs were not fixated from the CNT deposition process. Therefore a long time stability measurement was conducted by repeating the measurements after waiting a couple of days. The results where consistent with the expectations and the setup showed the nonlinear effects of the SA to gradually disappear.

Acknowledgements

I would like to give my sincere gratitude to my supervisor **Peter Zeil**, **Mikael Malmström** and **Niels Meiser** for their great amount of help with both answearing my questions and guidance of my project. My work would not have succeeded as well without them.

Many thanks I would like to give to my main supervisor **Valdas Pasiskevicius**, not only for coming up with this project but also for his expertice and feedback of my work and also to my examiner, **Lars-Gunnar Andersson** for his time on this project.

I would also like to thank my office mates **Oscar Frick**, **Robert Hurra**, **Robert Lindberg**, **Hoda Kianirad**, **Finn Klemming Eklöf**, **Riaan Stuart Coetzee** and **Junsong Peng** for their good company and help when discussing my project.

Many thanks to everyone at the laser physics group at Alba Nova for the good company and all the nice fika (coffee breaks), lunch breaks, small talk and many more pleasantries. My time here was great thanks to all of you!

And last I would also like to thank everyone again for all the interesting seminars and presentations I could attend to.

Contents

Chapter 1

Introduction

1.1 Background and Motivation

Fullerenes are molecules composed entirely of carbon, like graphene, buckminsterfullerene and carbon nanotubes (CNT)s. Of these carbon structures the latest studied is graphene, which won Andre Geim and Konstantin Novoselov the Nobel price in physics in 2010 [1].

Although the discovery of buckminsterfullerene (also called buckyballs) occurred in 1985, which won Robert F. Curl Jr, Sir Harold W. Kroto and Richard E. Smalley the Nobel price in 1996 [2], the first observation of these carbon structures were by Iijima in [3] five years earlier in 1980. These special round shaped structures can be thought of as folded graphene sheets forming a ball with hexagon and pentagon patterns similar to a football. Easier to imagine are the CNTs, which are constructed as rolled up graphene sheets.

With the first preparations of CNTs by Iijima in 1991 [4], CNT properties have been found useful in many fields, such as electrochemical sensors for deoxyribonucleic acid (DNA) detection in bioengineering [5] and transparent stretchable electronics [6], in which graphene share similar properties. The two main techniques of fabricating CNTs are the arc-discharge technique [7, 8] and the high-pressure carbon monoxide decomposition [9], both producing different tubule diameters but covering a broadband range in both cases. In electro optics they have been used for their intensity dependent absorption, with fast relaxation times (< 1 ps) for passive mode-locking [10] and are therefore a strong competitor to the semiconductor saturable absorber mirror (SESAM). The SESAM has been successfully used for mode-locking lasers at a similar time range with picosecond relaxation times [11].

With the use of spin-coating or other techniques, it is possible to integrate the CNTs or other carbon structures onto desired substrates. Song et al. [12] have successfully etched the surface of an optical fiber close to its core and thereafter spin-coated the surface in order to mode-lock with the evanescent field [**?**]. Although

carbon structures have proven to be a robust and low-cost alternative to other semiconductor-based saturable absorber (SA) for mode-locking of numerous laser architectures, the implementation of these structures in fiber lasers has so far relied on cumbersome trial-and-error approaches in order to determine suitable concentrations and geometries. In order to improve and simplify this process, this master thesis project aimed to realize a simple and reliable setup for direct characterization of the nonlinear absorption behavior of carbon structures deployed in fiber-based SA components. The evaluation of the setup was performed using fabricated fiber-based saturable absorbers where two methods were attempted. The first method used fibers with two holes surrounding the core allowing evanescent field interaction to be utilized when filling up the holes with SA. This method did not reach any conclusive results and the project instead tried deposition CNT using guided light to facilitate the attachment on the end-surface of single-mode fibers.

It shall be noted that although all methods described in the following chapters are suitable for all carbon structures, this project has focused its investigation only on CNTs.

1.2 Structure of the thesis

This is the end of the introduction chapter where the thesis layout will be summarized. In the next chapter the theory required to understand this thesis will be reviewed, including, light propagation in fibers, active and passive mode-locking and carbon nanotubes, specifically single-walled. The third chapter will describe the experimental work of the project, the fiber and CNT preparation with deposition of the CNTs, a review of the probe laser and the characterization setup with a detailed overview on how the measurement data is acquired. In chapter four the measurements are analyzed: both the data on the CNT deposition in sample preparation on fibers, along with the nonlinear transmission measurements of the setup. The final chapter will hold a conclusion of the work with an outlook for further investigation.

Chapter 2

Theory

This chapter consist of three introductory subjects, light propagation in optical fibers, mode-locking and CNTs. First an introduction in the theory of light propagation in optical fibers will be reviewed followed by mode-lock theory. Last a brief analysis will be given on CNTs.

2.1 Light propagation in fibers

Optical fibers commonly take advantage of total internal reflection (TIR) as guiding mechanism for optical signals. TIR occurs when light hits the boundary of an optically less dense material at an incident angle above the critical angle described in Snell's law (equation (2.1)), while propagating through a denser material [13].

$$n_1 \sin(\theta_1) = n_2 \sin(\theta_2). \tag{2.1}$$

The light will reflect on the surface and stay inside the optical dense medium as shown in figure 2.1, where n_0, n_1 and n_2 are the refractive indices of the surrounding medium, core and cladding respectively. Although it is enough to let light propagate through the denser medium and reflect on air, contact with any surfaces or dust particles will change the required conditions for TIR and start to leak light from the waveguide. Therefore even the most basic optical fiber always consists of at least two materials, the core with a higher refractive index n_1 and the cladding with a lower refractive index n_2 to ensure no leaking. These type of fibers are called step-index fibers due to the sudden change in refractive index along the fiber radius as shown in figure 2.2, which differ from graded-index fibers where the refractive index varies gradually along the radial axis.

Usually there is a third layer called the coating, which consists of a low-index acrylic compound that helps protect the very thin and fragile fiber and prevents any direct external contact with the cladding.

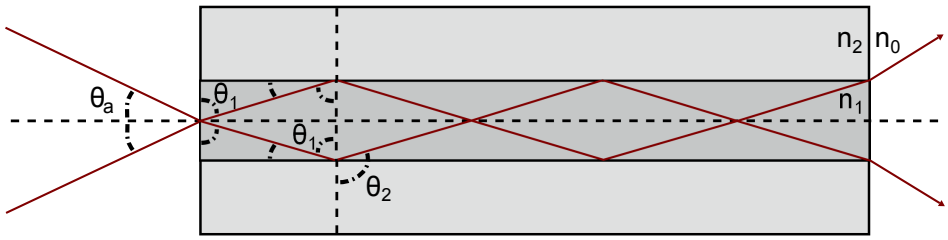

Figure 2.1: The cross section of an optical fiber along the wave-guiding axis with rays incident at the acceptance angle θ_a fulfilling the requirement for TIR.

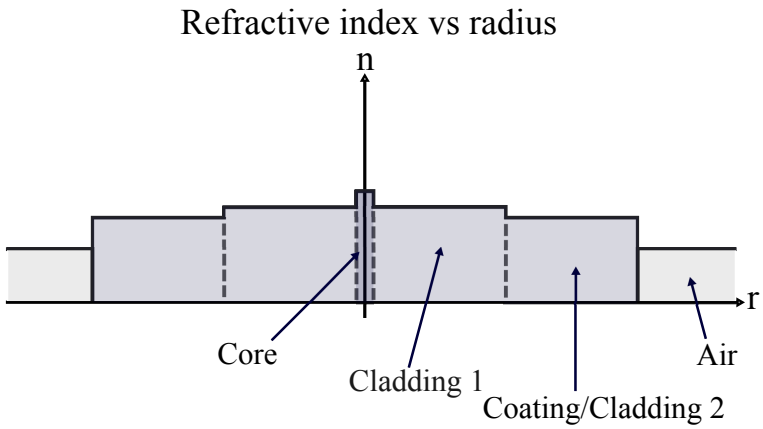

Figure 2.2: The diagram shows the refractive index variation along the radial direction of a step-index fiber.

Using equation (2.1) with the incidence angle reaching the critical angle $\theta_1 = \theta_c$, the critical angle can be described as $\theta_c = \arcsin(n_2/n_1)$ because $n_1 \sin(\theta_c) = n_2 \sin(\pi/2)$. For the case of $n_1 > n_2$, figure 2.1 shows that the maximum acceptance angle is reached when

$$\begin{aligned} &n_0 \sin(\theta_a) = n_1 \sin(\pi/2 - \theta_c) = n_1 \cos(\theta_c) = n_1 \sqrt{1 - \sin^2(\theta_c)} \Rightarrow \\ &\Rightarrow n_0^2 \sin^2(\theta_a) = n_1^2(1 - \sin(\theta_c)) = \left\{ \theta_c = \arcsin\left(\frac{n_2}{n_1}\right) \right\} = n_1^2(1 - \frac{n_2^2}{n_1^2}). \end{aligned} \tag{2.2}$$

Because of the critical angle required for TIR, only light that enters the core of the fiber within the acceptance angle will be contained. Therefore the numerical aperture (NA) of the fiber is defined from equation (2.2) which results in

$$\mathrm{NA} = n_0 \sin(\theta_a) = \sqrt{n_1^2 - n_2^2}, \tag{2.3}$$

where θ_a is the acceptance angle, n_0 is the surrounding medium, n_1 the core index and n_2 the cladding index [13]. A small NA therefore implies a small divergence angle and guides only light close to normal incidence, on the other hand a large NA allows light with larger incidence angles to be guided.

In waveguides there are only a limited amount of electrical field distributions allowed to be guided for the propagating light, which are called modes. By solving Maxwell's equation for light propagation in fibers, the NA and radius core a can be shown to affect the number of modes allowed to be guided and thus determine if a fiber operates in single-mode (SM) or multi-mode (MM) by using the V number, also known as the normalized frequency number, shown in equation (2.4).

$$V_{nr} = 2\pi\frac{a}{\lambda}\mathrm{NA} = 2\pi\frac{a}{\lambda}\sqrt{n_1^2 - n_2^2}, \tag{2.4}$$

where a is the core radius, λ the wavelength and NA the numerical aperture from equation (2.3), with the core and cladding indices and air as surrounding medium [14]. For the fiber to support only a single mode, it is necessary to have V $<$ 2.405, namely the first root of the Bessel function, J_0, due the solution of the wave equation for cylindrical mediums [15]. It is thus possible to achieve SM operation by either decreasing the core radius or index contrast when designing the fiber.

2.1.1 Dispersion and self-phase modulation

It is often only the linear part of the materials refractive index that is of interest for most applications, but there is also a second component which affects the nonlinear behavior of the material [15]. This term is referred to as the nonlinear refractive index which is often very small and will therefore only contribute at high intensities. In optical fibers nonlinear effects are often not negligible and must therefore be investigated in order to see how the propagating light will be affected.

The expression for the refractive index is therefore described in two parts as

$$\mathrm{n}(\omega) = \mathrm{n}_0(\omega) + \mathrm{n}_2(\omega)|E^2|, \tag{2.5}$$

where n_0 is the linear part, n_2 the nonlinear-index coefficient and $|E^2|$ is the intensity of the light with both terms depending on the frequency, ω, of the electric field. As the refractive index changes so does the effects on the propagating light, giving rise to a multitude of effects. Self-focusing for radial gradient beam profiles, is one example where the light starts to focus into its own center due to the radial changes of the refractive index.

The propagation constant and its wavelength dependency is shown in equation (2.6),

$$\beta(\omega) = n(\omega)\frac{\omega}{c} = \beta_0 + \beta_1(\omega - \omega_0) + \frac{1}{2}\beta_2(\omega - \omega_0)^2..., \tag{2.6}$$

where the Taylor series is expanded around the central frequency ω_0 and β_1 is inverse of the group-velocity dispersion (GVD), v_g, or proportional to the group index

$$\beta_1 = \frac{1}{v_g} = \frac{n_g}{c} = \frac{1}{c}\left(n + \omega\frac{dn}{d\omega}\right), \tag{2.7}$$

and the GVD parameter β_2, is the cause of pulse broadening due to dispersion of the group velocity

$$\beta_2 = \frac{1}{c}\left(2\frac{dn}{d\omega} + \omega\frac{d^2n}{d\omega^2}\right), \tag{2.8}$$

which can be related to the dispersion coefficient as

$$D = \frac{d\beta_1}{d\lambda} = -\frac{2\pi c}{\lambda^2}\beta_2 = -\frac{\lambda}{c}\frac{d^2n}{d\lambda^2}. \tag{2.9}$$

Due to β_2 being wavelength dependent, the sign of equation (2.9) can change for longer wavelengths in fused silica [15] and has therefore a certain wavelength where both β_2 and D vanish. This wavelength is called the zero-dispersion wavelength, denoted as λ_D. At this wavelength some dispersive effects will remain due to the third order dispersion (TOD) parameter β_3.

All the wavelengths $\lambda < \lambda_D$, yielding $\beta_2 > 0$, represents the normal-dispersion regime. In this regime all high frequency parts of a pulse will travel at a slower pace than the lower frequencies. For the anomalous-dispersion regime, where $\lambda > \lambda_D$ and $\beta_2 < 0$ the opposite applies, with slower low frequency components.

Pulses of high energy or very short widths will often get their shape and spectrum distorted with increased intensities and shorter widths. This is due to dispersion called GVD or because of nonlinear effects known as self-phase modulation (SPM). By investigating the nonlinear Schrödinger (NLS) pulse propagation equation (2.10) for SM fiber [15] where the higher terms have been removed, the most profound effect can be determined.

$$i\frac{\partial A}{\partial z} = -\frac{i\alpha}{2}A + \frac{\beta_2}{2}\frac{\partial^2 A}{\partial T^2} - \gamma|A|^2A, \tag{2.10}$$

A is the slowly varying amplitude of the pulse envelope, α is the absorption coefficient, β_2 the GVD parameter (see equation (2.6)) and T is measured in the co-moving frame of the pulse propagating at the group velocity v_g meaning the pulse center will always be at the zero point, as defined in equation (2.11).

$$T = t - \frac{z}{v_g}, \tag{2.11}$$

The last term of equation (2.10) contains γ which is the nonlinear coefficient defined as

$$\gamma(\omega_0) = \frac{n_2(\omega_0)\omega_0}{cA_{eff}}, \tag{2.12}$$

where n_2 is the nonlinear refractive index, ω_0 the carrier frequency and A_{eff} the effective mode area defined as

$$A_{eff} = \frac{\left(\iint_{-\infty}^{\infty} |F(x,y)|^2\, dxdy\right)^2}{\iint_{-\infty}^{\infty} |F(x,y)|^4\, dxdy}, \tag{2.13}$$

If the mode area is approximated to be Gaussian distributed, i.e $F(x,y) \approx \exp[-(x^2+y^2)/w^2]$ where w is the width parameter, the effective area becomes $A_{eff} = \pi w^2$.

On the right hand side of equation (2.10), starting from the left, the terms describe fiber loss, dispersion and SPM in the fiber. Depending on the magnitude of the pulse width T_0 related to the pulse full width at half-maximum (FWHM) τ_p by

$$\mathrm{T}_0 = 2(ln2)^{1/2}\tau_p, \tag{2.14}$$

and the peak power P_0 of the initial pulse, spectral and temporal broadening will be dominated to a varying degree by either dispersive or nonlinear effects [15].

If the time scale in equation (2.11) is normalized to the initial pulse width as

$$\tau = \frac{T}{\mathrm{T}_0} = \frac{t - z/v_g}{\mathrm{T}_0}, \tag{2.15}$$

and the amplitude in equation (2.10) gets normalized by replacing amplitude $A(z,t)$ using

$$A(z,t) = \sqrt{P_0}\exp(-\alpha z/2)U(z,t). \tag{2.16}$$

The normalized amplitude $U(z,\tau)$ can then be used together with equation (2.15) in order to get

$$i\frac{\partial U}{\partial z} = \frac{\mathrm{sgn}(\beta_2)}{2\mathrm{L}_D}\frac{\partial^2 U}{\partial \tau^2} - \frac{\exp(-\alpha z)}{\mathrm{L}_{NL}}|U|^2 U, \tag{2.17}$$

where L_D and L_{NL} are the dispersive and nonlinear lengths defined as

$$\mathrm{L}_D = \frac{\mathrm{T}_0^2}{|\beta_2|}, \tag{2.18}$$

where β_2 is the GVD parameter and shows what length the pulse needs to propagate in order to broaden by a factor of $\sqrt{2}$.

The nonlinear length is in turn defined as

$$\mathrm{L}_{NL} = \frac{1}{\gamma P_0}, \tag{2.19}$$

where P_0 is the peak power.

In order to demonstrate the phase shift induced from the phenomenon of SPM, equation (2.17) can be solved with neglected dispersion ($\beta_2 = 0$) for simplicity, which gives

$$\frac{\delta U}{\delta z} = \frac{i \exp(-\alpha z)}{\mathrm{L}_{NL}} |U|^2 U. \tag{2.20}$$

By expressing the amplitude as $U = V \exp i\Phi_{NL}$ the derivative becomes

$$\frac{\delta V}{\delta z} \exp(i\Phi_{NL}) + i\frac{\delta \Phi_{NL}}{\delta z} V \exp(i\Phi_{NL}) = i\frac{\exp(-\alpha z)}{\mathrm{L}_{NL}} |V|^2 V \exp(i\Phi_{NL}). \tag{2.21}$$

From this it is evident that $\frac{\delta V}{\delta z} = 0$ and $\frac{\delta \Phi_{NL}}{\delta z} = \frac{\exp(-\alpha z)}{\mathrm{L}_{NL}} |V|^2$, integration thus gives the solution

$$\begin{aligned} &V = V_0(t), \\ &\Phi_{NL} = \frac{\exp(-\alpha z)}{-\alpha \mathrm{L}_{NL}} |V_0(t)|^2 + C \\ &z = 0 \Rightarrow C = |V_0(t)|^2 / \alpha \mathrm{L}_{NL}, \end{aligned} \tag{2.22}$$

which leads to

$$\begin{aligned} U(z,t) = V_0(t) \exp(i\Phi_{NL}) = V_0(t) \exp\left(i \left(C + \frac{-\exp(-\alpha z)}{\alpha \mathrm{L}_{NL}} \right) |V_0(t)|^2 \right) \Rightarrow \\ \Rightarrow \quad \{U(0,t) = V_0(t)\} \quad \Rightarrow U(z,t) = U(0,t) \exp\left(i \frac{1 - \exp(-\alpha z)}{\alpha \mathrm{L}_{NL}} |U(0,t)|^2 \right). \end{aligned} \tag{2.23}$$

The nonlinear phase shift is therefore defined as $\Phi_{NL} = (1 - \exp(-\alpha z))/(\alpha \mathrm{L}_{NL})|U(0,t)|^2)$ which for negligible absorption ($\alpha = 0$) can be written as $\Phi_{NL} = z/\mathrm{L}_{NL}|U(0,t)|^2)$. For a fiber of length L this thus becomes

$$\Phi_{NL} = \mathrm{L}/\mathrm{L}_{NL}|U(0,t)|^2. \tag{2.24}$$

2.1.2 Dispersive and nonlinear regime

In order to see which effects are most dominant, some estimations can be used to see at what fiber lengths certain effects have the most impact. For dispersive effects to have the major influence in the fiber, the pulse needs to travel a length close to, or higher, than the dispersion length in equation (2.18).

For the case of a fiber length L smaller than both the nonlinear length ($\mathrm{L} \ll \mathrm{L}_{NL}$) and dispersive length ($\mathrm{L} \ll \mathrm{L}_D$), the contributions from the nonlinear and dispersive effects will have a smaller influence, as can be seen in equation (2.17) where both of the right hand side terms becomes comparatively small. The shape of the beam profile will therefore not change during its propagation and $U(z,\tau) = U(0,\tau)$, but the fiber will still have absorption losses.

Continuing with the case of $\mathrm{L} \ll \mathrm{L}_{NL}$ and $\mathrm{L} \sim \mathrm{L}_D$, the dispersive effects will be more evident as the nonlinear part of equation (2.17) becomes negligible. The pulse shape during propagation is considered to be in the dispersion-dominant regime and will therefore broaden due to GVD as long as equation (2.25) holds true.

$$\frac{\mathrm{L}_D}{\mathrm{L}_{NL}} = \frac{\gamma P_0 T_0^2}{|\beta_2|} \ll 1. \tag{2.25}$$

Similar to the previous case, when $\mathrm{L} \sim \mathrm{L}_{NL}$ and $\mathrm{L} \ll \mathrm{L}_D$, the dispersion term becomes negligible (with the assumption that the temporal profile of the pulse is smooth such that $\partial^2 U/\partial\tau^2 \sim 1$ [15]). In this nonlinearity-dominant regime the pulse spectrum will change due to SPM and is applicable when equation (2.26) is satisfied.

$$\frac{\mathrm{L}_D}{\mathrm{L}_{NL}} = \frac{\gamma P_0 T_0^2}{|\beta_2|} \gg 1, \tag{2.26}$$

If both the nonlinear length and the dispersive length are comparable to the fiber length, $\mathrm{L} \sim \mathrm{L}_{NL}$ and $\mathrm{L} \sim \mathrm{L}_D$, both GVD and SPM effects will affect the pulse evolution in different ways depending on the sign of the dispersion parameter β_2 which can be seen in equation (2.17). In the normal-dispersion regime where $\beta_2 > 0$, high frequencies are forced to travel at a slower pace compared to lower frequencies and can be used together with SPM effects to compress the pulse by creating new frequency components and therefore compressing the pulse. While in the anomalous-dispersion regime, where the low frequencies travels at a slower pace,

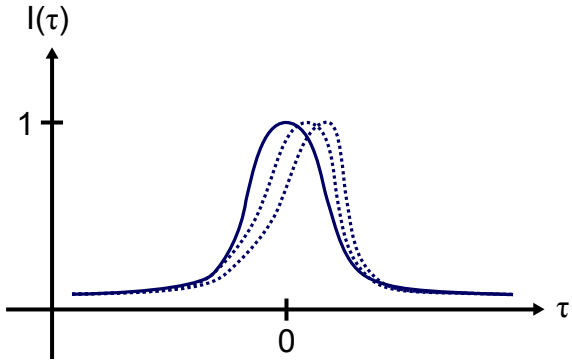

Figure 2.3: The figure depicts a pulse with normalized intensity whose shape deforms for the dispersion and absorption-less case, where the solid line is for the starting position $Z = z/\mathrm{L}_{NL} = 0$, with increasing distance Z for the dashed curves.

the GVD effects along with the SPM will start to cancel the broadening for both the pulse width and spectrum, therefore maintaining the pulse shape throughout the propagation. For both cases there are requirements on the intensity, spectrum and nonlinearity parameters that needs to be fulfilled.

2.1.3 Self-steepening and self-focusing

Optical fibers guiding high power pulses, additional nonlinear effects can come to affect the beam profile or pulse shape. Example of such nonlinear effects can be self-steepening and self-focusing, which are going to be described briefly in this section.

The pulse shape can be deformed depending on intensity due to the intensity dependent group velocity which will make the high intensity peak pulse center to become slower than the leading edge and therefore slowly shift to the trailing edge as shown in figure 2.3. This effect is called self-steepening and occurs at higher intensities, which can be demonstrated by looking at the NLS equation (2.27), which is similar to the previously mentioned equation (2.10), but with the higher terms included.

$$\frac{\delta A}{\delta z} + \frac{\alpha}{2}A + i\frac{\beta_2}{2}\frac{\delta^2 A}{T^2} - \frac{\beta_3}{6}\frac{\delta^3 A}{\delta T^3} = i\gamma\left(|A|^2 A + \frac{i}{\omega_0}\frac{\delta}{\delta T}\left(|A|^2 A - T_R\frac{\delta|A|^2 A}{\delta T}\right)\right). \tag{2.27}$$

Assuming negligible absorption $\alpha = 0$, dispersion $\beta_2 = \beta_3 = 0$ and $T_R = 0$ which relates to the Raman-induced frequency shift [15], the NLS becomes

$$\frac{\delta A}{\delta z} = i\gamma\Big(|A|^2 A + \frac{i}{\omega_0}\frac{\delta}{\delta T}(|A|^2 A)\Big). \tag{2.28}$$

Introducing the amplitude normalization from equation (2.16) together with equations (2.15), (2.19) and using $Z = z/\mathrm{L}_{NL}$ into equation (2.28) results in

$$\frac{\delta U}{\delta Z} = i|U|^2 U - s\frac{\delta}{\delta\tau}\left(|U|^2 U\right), \tag{2.29}$$

where the term $s = \frac{1}{\omega_0 \mathrm{T}_0}$ governs the self-steepening. Similar to previous rewriting of the amplitude with a phase term, $U = \sqrt{I}\exp(i\phi)$ can be used in order to get equation (2.29) separated into a real and imaginary part where the equation below can be obtained [15].

$$\begin{aligned} &\frac{\delta I}{\delta Z} + 3sI\frac{\delta I}{\delta + \tau} = 0, \\ &\frac{\delta \phi}{\delta Z} + sI\frac{\delta \phi}{\delta \tau} = I. \end{aligned} \tag{2.30}$$

The general solution to equation (2.30) results in a shape function which depends on the intensity and the self-steepening term s shown below.

$$I(Z,\tau) = f(\tau - 3sIZ) \tag{2.31}$$

For $Z = 0$ the function becomes $f(\tau)$ and will show an increase in steepening over time, as shown previously in figure 2.3 where the solid line depicts the case for $Z = z/\mathrm{L}_{NL} = 0$, with increasing Z for the dashed and dotted lines. The shift of the pulse center from self-steepening will cause asymmetric spectrum broadening in SPM [15].

The intensity dependent refractive index can give rise to more effects than the previously discussed. One such effect called self-focusing can make the propagation material to act like a positive lens.

Considering the case of light freely propagating through vacuum at a time t_0 in the axial direction z with a radial decreasing intensity $I(r)$, to suddenly hit a material with refractive index $n(I)$ at vertical incidence angle in time t_1 as depicted in figure 2.4. Due to the intensity dependent refractive index the parts of the beam with high intensity will give rise to a higher refractive index, effectively giving the material the property of a positive lens and thus giving the name to the phenomena of self-focusing.

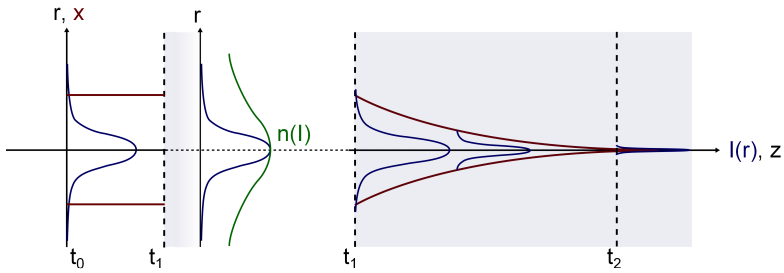

Figure 2.4: A beam propagating through vacuum until hitting a material with refractive index $n(I)$ at incidence angle. Due to the intensity dependency, the material will act as a positive lens, converging the beam.

2.2 Mode-locking

By using light amplification by stimulated emission of radiation (laser), highly coherent light sources can be achieved. Inside the laser cavity where the amplification occurs, there are sets of both longitudinal and transversal modes the cavity can support depending on the shape and symmetry of the resonator. Usually these modes oscillate at random phases giving an oscillating pattern for all continuous wave (CW) laser sources. Showing in figure 2.5 is the time dependency of an example output beam where the square of the electric field amplitude $|A(t)|^2$ is normalized with the square of the electric amplitude E_0 for $N = 51$ oscillating consecutive longitudinal modes, whose phases are assumed to be fixed between all modes [16]. In this case each mode has an equal amplitude of E_0, separated with a fixed frequency $\Delta v = c/2\mathrm{L}$ between each other, where L is the cavity length. Although the output beam looks to be completely at random this shape will remain same provided the real phase relation between the modes stay constant after each round-trip in the cavity and therefore the oscillating waveform will be periodic with $\tau_p = 1/\Delta v$ [16]. The total oscillating bandwidth will then be $\Delta v_L = N\Delta v$, where each pulse in the oscillating waveform has a width of approximately $1/\Delta v_L$, which will be shown later in equation (2.39).

If the phase of the oscillating pulses can be fixed between each mode, interference between the modes can result with the CW pattern to become pulsed with very short durations in the order of picoseconds or femtoseconds.

2.2.0.1 Time-domain picture

There are different ways to achieve mode-locked lasers and the basic concept is to get the strongest pulse in the oscillating waveform in figure 2.5 to survive in the cavity, meaning that only one will get amplified from the gain while letting the other pulses decay. One way is to introduce some periodic loss or block, imagine a shutter for example, that is set next to the output coupler with an opening period of $\mathrm{T} = 2\mathrm{L}/\mathrm{c}$ where L is the cavity length, making this the cavity round-trip

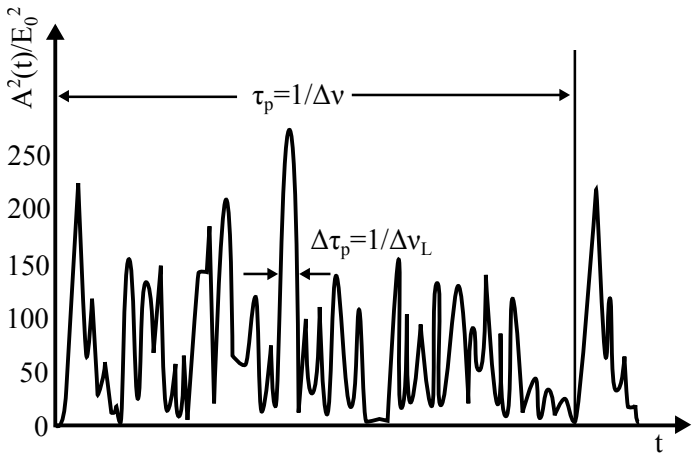

Figure 2.5: The oscillating modes in the cavity of a laser, with pulse width $\Delta\tau$ and periodicity τ_p [16].

time. If the shutter only lets one pulse propagate, preferably the strongest one, the rest of the pulses in the waveform will decay. This will also create a spacing of 2L/c between the pulses which is the fundamental mode-locking repetition rate [16]. Depending on where the shutter is positioned in the cavity it is possible to achieve harmonic mode-locking where the opening period will be increased to $T = 4L/c$ and $T = 6L/c$ for position L/c and 2L/3c respectively. This will allow more pulses from the waveform to survive and resonate within the cavity thus also increasing the repetition rate of the output pulses. Although no short active shutter exists, different kinds of modulators are used instead. It is often preferred to use a sinusoidal modulation function in order to mode-lock in this manner, which will be discussed later in section 2.2.1.

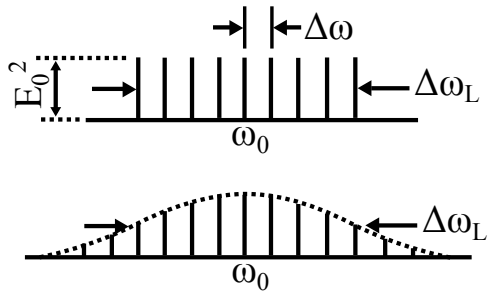

Figure 2.6: Above are shown two examples of mode amplitudes versus frequency for a mode-locked laser with a frequency spacing of $\Delta\omega$ and a bandwidth of $\Delta\omega_L$. The first example shows a uniform mode amplitude distribution while the lower depicts a Gaussian distributed case [16].

2.2.0.2 Frequency-domain picture

Looking at the frequency spectrum of a mode-locked output beam will show all consecutive longitudinal modes separated with a frequency of $\Delta\omega$, bandwidth of $\Delta\omega_L$ and central frequency of ω_0. Following the example of figure 2.6, where all modes have equal amplitude E_0, in order to achieve mode-locking, their phases have to be locked with a constant phase of φ [16] and the following relation

$$\varphi_k - \varphi_{k-1} = \varphi. \tag{2.32}$$

This means that the phase difference between each mode is φ with a total of $(2n + 1) = l$ longitudinal modes.

2.2.0.3 Equal amplitude distribution

Looking into the frequency perspective of mode-locking, the electric field of the output beam can be described as

$$E(t) = \sum_{k=-n}^{n} E_0 \exp[j(\omega_0 + k\Delta\omega)t + k\varphi], \tag{2.33}$$

where the sum encloses the central mode at $k = 0$. This can we rewritten as

$$E(t) = A(t)\exp(j\omega_0 t) \qquad A(t) = \sum_{k=-n}^{n} E_0 \exp[jk(\Delta\omega t + \varphi)]. \tag{2.34}$$

with a time dependent amplitude $A(t)$. $E(t)$ can therefore be seen as a sinusoidal wave with center frequency ω_0 [16].

By introducing the substitution $\Delta\omega t' = \Delta\omega t + \varphi$, remembering that φ is constant when the phase-locking condition (equation 2.32) is applied and therefore assuming the output is mode-locked, the amplitude can be written as

$$A(t') = \sum_{k=-n}^{n} E_0 \exp[j(k\Delta\omega t')]. \tag{2.35}$$

Utilizing the geometrical progression

$$\begin{aligned} &\sum_{k=-n}^{n} ar^k \Rightarrow (1-r)\sum_{k=-n}^{n} ar^k = (1-r)(ar^{-n} + ... + ar^0 + ... + ar^n) \Rightarrow \\ &\Rightarrow A(t') = \sum_{k=-n}^{n} ar^k = \frac{a(r^{-n} - r^{n+1})}{1-r}, \end{aligned} \tag{2.36}$$

for a = E_0 and $r = e^{j(\Delta\omega t')}$ the end result is

$$A(t') = E_0 \frac{\sin((2n+1)\Delta\omega t'/2)}{\sin(\Delta\omega t'/2)} \tag{2.37}$$

Examining equation (2.37) it is clear from the relation of l'Hopital's rule $\lim_{x\to\pi} \frac{\sin(ax)}{\sin(x)} = a$ [17], that each time both the nominator and denominator vanishes the waveform will have achieved its peak with all of the mode amplitudes in phase with each other. Each pulse will therefore constructively interfere with a period of $\Delta\omega t'/2 = \pi$ and oscillate near zero the rest of the times. This will therefore result in a temporal separation of each pulse with the time of

$$\tau_p = \frac{2\pi}{\Delta\omega} = \frac{1}{\Delta\nu}, \tag{2.38}$$

where $\Delta\nu$ is the frequency separation for each pulse shown previously in figure 2.5.

Using equation (2.37) again and comparing the phases of the modes, each will have their own phase speed where all will coincide destructively for each period of $(2n+1)\Delta\omega t'/2$. Due to this the amplitude in equation (2.37) vanishes at a time t'_p where $(2n+1)\Delta\omega t'_p/2 = \pi$. Now since the time t'_p and the FWHM $\Delta\tau_p$ of the $A^2(t')$ peaks are roughly the same (see figure 2.7). Therefore can t'_p be approximated as $\Delta\tau_p$,

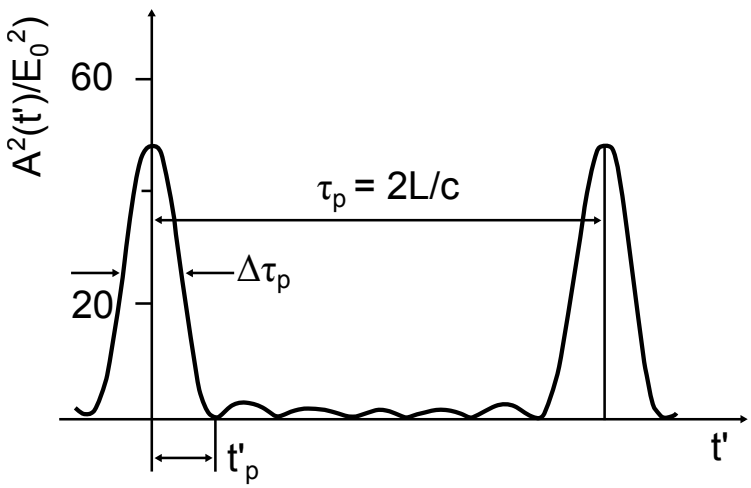

Figure 2.7: The case of seven oscillating modes with locked phases from the case in figure 2.6 [16].

$$t'_p \cong \Delta\tau_p = \frac{2\pi}{(2n+1)\Delta\omega} = \frac{1}{\Delta\nu_{\mathrm{L}}}, \tag{2.39}$$

where $\Delta\tau_p$ is the pulse FWHM width and $\Delta\nu_\mathrm{L}$ the total bandwidth. This shows that with more phase locked modes, the shorter pulses can be achieved when mode-locking.

2.2.0.4 Gaussian distributed modes

So far only the simplified case of having equal amplitude for all modes has been discussed, which is unrealistic since the gain profile is determined by the mode amplitude envelope. Normally each mode would therefore differ in amplitude, where instead of having a rectangle envelope function, it would be more common to have a Gaussian distribution as in the latter example in figure 2.6. The electric amplitude for mode k can for the Gaussian case be written as

$$E_k^2 = E_0^2 \exp[-(2k\Delta\omega/\Delta\omega_\mathrm{L})^2 \ln 2], \tag{2.40}$$

where as previously mentioned $\Delta\omega_\mathrm{L}$ is the spectral bandwidth and $\Delta\omega$ the frequency separation [16]. Assuming that the phase condition in equation (2.32) is fulfilled and the central mode has zero phase, $\varphi_0 = 0$, this can be written as previously shown in equation (2.34) giving

$$A(t') = \sum_{k=-\infty}^{\infty} E_k \exp[jk(\Delta\omega t')]. \tag{2.41}$$

The amplitude $A(t)$ is proportional to the Fourier spectral amplitude E_k if the sum in equation (2.41) is approximated to an integral [16]. The pulse intensity $A^2(t)$ will still be a Gaussian function of time

$$A^2(t) \propto \exp[-(2t/\Delta\tau_p)^2 \ln 2] \qquad \Delta\tau_p = \frac{2\ln 2}{\pi\Delta\nu_\mathrm{L}} = \frac{0.441}{\Delta\nu_\mathrm{L}}, \tag{2.42}$$

where $\Delta\tau_p$ is the FWHM of the pulse intensity.

The two cases with the different mode-amplitude envelopes in figure 2.6 have shown that the pulse duration $\Delta\tau_p$ can be related to the spectral bandwidth $\Delta\nu_\mathrm{L}$ along with a numerical factor β as $\Delta\tau_p = \beta/\Delta\nu_\mathrm{L}$. β depends on the shape of the spectral distribution shown in figure 2.6 and yields $\beta = 1$ for the rectangular envelope and $\beta = 0.441$ for the Gaussian envelope. Pulses that follow these relations are called transform-limited [16]. It is possible to have mode-locking conditions other from equation (2.32) which are non-linear, for example $\varphi_k = k\varphi_1 + k^2\varphi_2$ where φ_1 and φ_2 are constants. In this case the pulse will not be transform-limited and will produce a frequency chirped pulse.

2.2.1 Active mode-locking

The three main methods of active mode-locking are amplitude modulation (AM) (modulation of the pulse amplitude), frequency modulation (FM) (modulation of the pulse phase) and synchronous pumping where the laser gain is modulated with a frequency matching the fundamental cavity frequency $\Delta\nu = c/2L$ so that the pulse passes when the losses are at their minimum [16]. The AM mode-locking will be reviewed since it is the most common method.

Considering the case when a modulator (where the time varying loss is at a minimum at frequency ω_m) is inserted into the laser cavity, the electric field $E_k(t)$ can be described as

$$\begin{aligned} E_k(t) &= E_0(1-\delta/2(1-\cos(\omega_m t)))\cos(\omega_m+\phi_k), \\ E_k(t) &= E_0(1-\delta/2)\cos(\omega_k t+\phi_k)+\delta/4[\cos((\omega_k+\omega_m)t+\phi_k)+ \\ &+\cos((\omega_k-\omega_m)t+\phi_k)]), \end{aligned} \tag{2.43}$$

with the amplitude being suppressed from E_0 to $E_0(1-\delta)$ where δ is the depth of the modulation function. It can be seen in the last step in equation (2.43) that there are two oscillating side bands at $\omega_k \pm \omega_m$. When $\omega_m = \Delta\omega = 2\pi\Delta\nu$, where $\Delta\nu$ is the frequency spacing between longitudinal modes, these modulation side bands will coincide with the cavity modes [16].

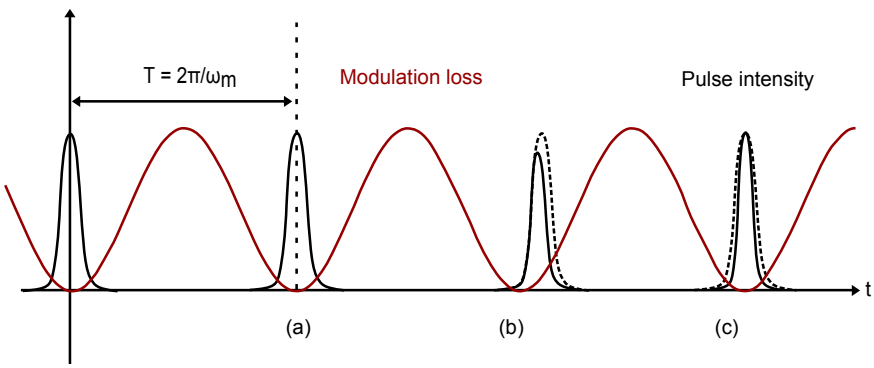

Figure 2.8: The time dependence of AM shown for a pulse in (a) steady-state, (b) a pulse with a time miss-match from the minimum loss time and (c) the pulse experiencing shortening and broadening, to finally reach steady-state.

In figure 2.8 the cavity pulses are shown to be in steady-state in part (a), where the periodicity of the modulation losses has coincided with the cavity round-trip time. If the pulse center is misplaced relative to the modulation function minimum loss time, then the sideband will be suppressed, pushing the pulse center closer to the minimum loss time of the modulator. Showing in figure 2.8 (b) is the dashed pulse which will be brought closer to the minimum of the modulation loss for each

round-trip shown as the solid line. When the pulse center has coincided with the minimum loss time (c), the pulse will continue to get shortened by the same process of the sideband suppression from the modulation loss until limited by the gain bandwidth and modulation depth but normally the bandwidth limit is not reached in AM.

2.2.2 Passive mode-locking

Unlike active mode-locking where the modulator needs to be actively feed an external source in order to control the modulation, passive mode-lockers will respond to the laser signal without any external input and therefore only need to be designed to match the gain and loss conditions for mode-locking (although GVD and SPM can be contributing effects). Active mode-locking utilizes a sinusoidal modulation function with a frequency of the repetition rate, where the low-loss window will be longer compared to passive mode-locking and therefore also generating longer pulses.

A common method for passive mode-locking is the use of a SA to modulate the cavity pulses. All SA have a nonlinear interaction depending on intensity, saturating the absorption with higher intensity for the absorbing wavelengths and therefore lowering the losses. This effect can be used to repress the low intense cavity modes in figure 2.5 due to the round-trip cavity loss being greater than the gain. The most intense peak will therefore survive and start to grow after several cavity round-trips if certain conditions are met[18].

SA can be divided into two groups, *Fast saturable absorbers* and *Slow saturable absorber* where the distinct difference is only in their relaxation time.

In figure 2.9, where the red line corresponds to the round-trip cavity loss and the green to the gain, it is demonstrated for a mode-locked situation how the fast and slow saturable absorber will create a time window where gain is higher than the loss from the absorbers, allowing the highest mode to resonate in the laser cavity. With increasing pulse intensity the loss due to the SA will decrease and in a certain span, be lower than the cavity gain. This will create a time window where it is possible to form pulses.

For the fast saturable absorber the loss change will be directly visible with change of intensity, in contrast to the slow saturable absorber where the absorption has saturated and at a slower pace will go back to the relaxed state as seen in figure 2.9. Similar to mode-locking with amplitude modulation discussed in the previous section, the pulse tails are formed due to the pulse broadening mechanism of the finite gain bandwidth, while the modulation compresses the pulse reaching an equilibrium.

Example of a fast saturable absorbers are the semi-conducting CNTs and have been demonstrated to mode-locked lasers with relaxation times measured to be < 1 ps [10].

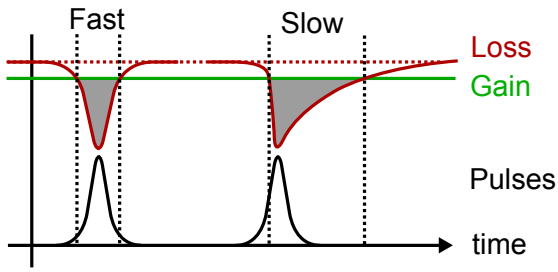

Figure 2.9: The red line depicts round trip cavity loss, the green is the gain with the assumption that no gain saturation occurs. The gray area is where the gain has exceeded the losses and can form the pulses. The two cases for the fast and slow SA are shown on the left and right side respectively.

2.3 Carbon Nanotubes

The research area of nanotechnology got greatly fueled and a high interest formed for carbon nanotubes ever since Sumio Iijima first showed the synthesis of carbon nanotubes using an arc-discharge evaporation method in 1991 [4]. Due to his work, Iijima has been proclaimed as the inventor of carbon nanotubes.

CNTs can be categorized into two groups, single-walled CNTs and multi-wall CNTs.single-wall carbon nanotubes (SWCNT)s are composed by, as the name imply, a single wall of CNTs while multi-wall carbon nanotubes (MWCNT)s are composed by several tubes surrounding one another. Both the amount of layers as well as the chirality of the carbon nanotubes constitutes their physical behavior. Iijima based his work on the former type of CNTs, the MWCNTs.

2.3.1 Single-walled carbon Nanotubes

A SWCNT can be described as a rolled up graphene sheet where the chiral angle determines the orientation axis of how the sheet was rolled, see figure 2.10. The tube diameter and chiral angle will affect the electronic properties of CNTs introducing either metallic or semi-conducting properties. [19]. With their electrical properties dependent on the wrapping angle, it is convenient to categorize them into three groups of different chirality, armchair, zigzag and chiral shown in figure 2.11.

As seen in figure 2.10 the angle changes depending on how the sheet was rolled. The two edges have to coincide on equivalent sites of the lattice in order form a tube. Therefore the only wrapping angles allowed are determined by the two integers m and n. These integers form the wrapping vector $\mathbf{C} = \mathrm{n}\mathbf{a}_1 + \mathrm{m}\mathbf{a}_2$ which determines the site where the edges coincide, where $\mathbf{a}_1$ and $\mathbf{a}_2$ are the unit vectors [19]. The wrapping vector therefore defines the diameter of the CNTs.

If the wrapping angle is $\theta = 0°$ (or $\mathrm{m} = 0$) the tube is called zigzag and for $\mathrm{n} = \mathrm{m}$ it is called armchair. Anything in between is called chiral with angles between $0° < \theta < 30°$. According to Wilder [19], using the energy dispersion relation for

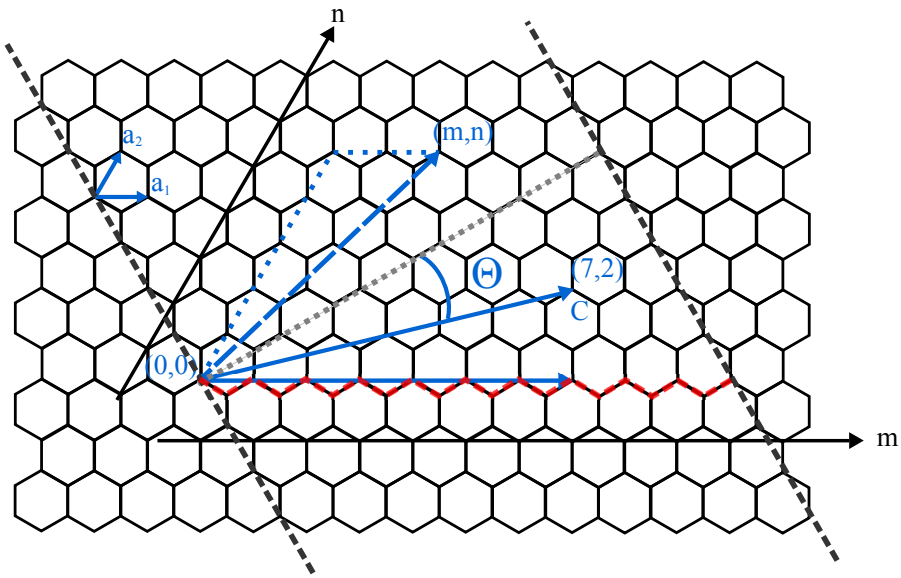

Figure 2.10: The chirality is determined in which way the grahpene sheet is rolled. The possible ways to roll the carbon sheet are determined by the wrapping vector $\mathbf{C} = n\mathbf{a}_1 + m\mathbf{a}_2$, where $\mathbf{a}_1$ and $\mathbf{a}_2$ are the unit vectors and m and n are integers. This way the two edges will coincide and form a tube.

a two dimensional graphene sheet and applying periodic boundary conditions the energy dispersion relations for the tube can be derived. The calculations predicted metallic behavior for armchair tubes (n = m) due to bands crossing the Fermi level. For both the chiral and zigzag tubes there are two possibilities. If their wrapping vector follows the relation n - m = $3l$, where l is an integer, the CNTs obtain metallic properties, while for n - m $\neq 3l$ they will obtain semi-conducting properties, with a band gap in the order of 0.5 eV. The exact value of the band gap is in turn determined by the diameter of the CNTs, as shown in equation (2.44)

$$\varepsilon_{\text{gap}} = 2\gamma_0 \frac{a_{\text{c-c}}}{d}, \tag{2.44}$$

where ε_{gap} is the band gap energy, γ_0 is the C-C tight-binding overlap energy, $a_{\text{c-c}}$ is the distance to the nearest carbon neighbor (0.142 nm) and d the diameter of the tube [20].

The absorption and emission spectra have been studied for different types of CNTs showing the band gap diameter dependence [21]. Figure 2.12 illustrates the emission and absorption transitions as E_{11} and E_{22}. The exact location of the levels depends on the nanotube diameter as previously mentioned.

Since even small changes of the CNTs diameter induce large variations in the

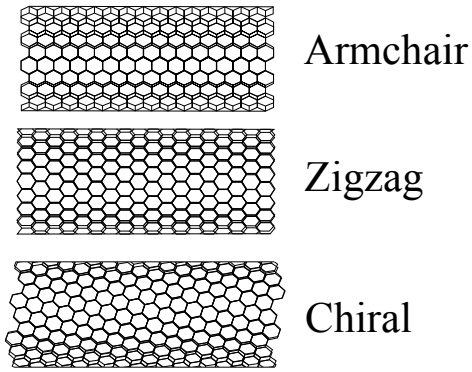

Figure 2.11: The three different types of SWCNT, Armchair with m = n, Zigzag m = 0 or $\theta = 0^\circ$ and Chiral with $0^\circ < \theta < 30^\circ$, where m and n are integers.

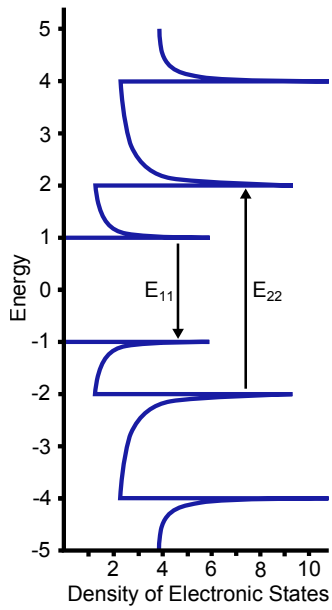

Figure 2.12: The energy levels and states for a CNT where the emission E_{11} and absorption E_{22} transitions are shown. The exact position of the energy levels depends on the diameter of the CNT.

band gap, CNTs in general have a broad spectrum introduced from small changes in the diameter due to the fabrication process.

CNTs with an average diameter of 1.4 nm, created using the arc-discharge method, where integrated into a low absorption host material and measured to have

strong absorption around 1800 nm and 1000 nm. These CNTs have successfully been used as SA in order to mode-lock a semiconductor disk laser [22]. A CNT diameter of 1.4 nm was manufactured by Journet [7], although it is possible to decrease the diameter to 0.93 nm [23]. For these reasons, CNTs cover a broad spectrum and are a cheap material to use for mode-locking.

Chapter 3

Preparation and characterization of fiber-integrated CNTs

During this project two fibers were available for use, which are going to be described after the CNT preparation process in the first part of this chapter. Next, both the sample design and the parameters of the two fibers will be discussed, concluding with reviewing the different CNT attachment methods for each fiber type.

3.1 Preparation of the carbon nanotubes

The CNT solution used in this project contained a CNT concentration of 0.1 mg/ml and was dispersed in 1.2-dichlorobenzene (DCB) along with a surfactant. All CNT solutions were centrifuged for 30 minutes at 20 000 relative centrifugal force (rcf) prior to use, separating the ashes from the tubes. The ashes accumulated for about 1/3 of the container, leaving the top 2/3 of the solution with CNTs.

A solution with CNTs and poly(methyl methacrylate) (PMMA) was prepared with the purpose of filling a two-hole fibers, which compared to a solution with only CNTs, has the advantage of permanently attach the CNTs within the host material. At first, a PMMA solution containing no CNTs was prepared by diluting it with DCB while stirring on a heat plate at 45 C° until the concentration of the PMMA reached 10%. The CNT solution was added afterwards with a desired amount, which was tested for a 1:1 ratio.

3.2 Fiber sample design

Two different fibers were available during this project, the commercially available HI 1060 fiber [24] and a two-hole fiber. First, the two-hole fiber will be discussed following by the HI 1060 fiber.

3.2.1 Two-hole fibers

As can be seen in figure 3.1, the fiber has two asymmetrical holes around the center, where one hole is closer to the core than the other. The main idea is to let the fiber core guide the pulses through the core and letting the evanescent field interact with the CNTs in the hole closest to the core. This is similar to the d-shaped fibers of Song [**?**] where the evanescent field interacts with the spin-coated CNTs, but with integrated CNTs in a reproducible manner.

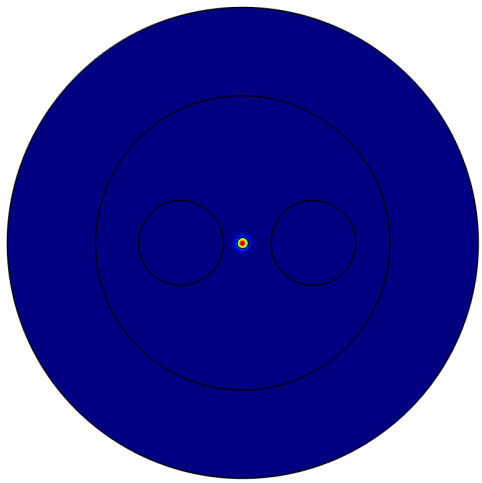

Figure 3.1: This COMSOL Multiphysics model shows the electric field distribution of a single mode being guided for wavelength 1040 nm. The outer circle represents the coating, the inner circle being the cladding and the core guiding the single mode is in the center of the model. There are two other circles around the core which represents the holes of the fiber. For comparison see figure 3.2b.

The effective mode area for the two-hole fiber was measured using two pictures of the fiber-end, one where the cladding is visible and one with a clear view of the core and unsaturated pixels shown in figure 3.2. The core profile was plotted from the unsaturated picture and the scaling corrected using the picture of the cladding, which is known to be 125 μm in diameter. With the FWHM being 4.4 μm the effective area is $A_{eff} \approx \pi 2.2^2 \approx 15\ \mu\text{m}^2$ which will be used to determine the the fluence.

Table 3.1: Some parameters of the SM fiber which was labeled two-hole fiber due to the two holes around the core.

Cladding Outer Diameter	125 μm
Core Diameter	4.8 μm
Hole Diameter	36 μm
Min. distance core-hole edge	9.6 & 5.8 μm
Hole edge from core center	12 & 8.2 μm
Effective Mode area	15 μm^2

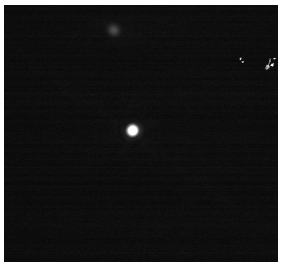

(a) The core of a di-hole fiber is clearly shown above, with no saturated pixels.. The white spots in the upper right corner are damaged parts of the sensor.

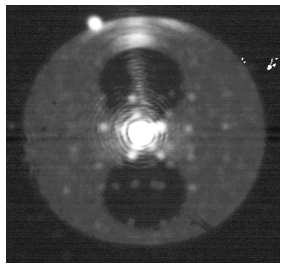

(b) The cladding is visible in this image and known to be 125 μm in diameter. Note the pixels are saturated in the core and can therefore not be used to plot its profile.

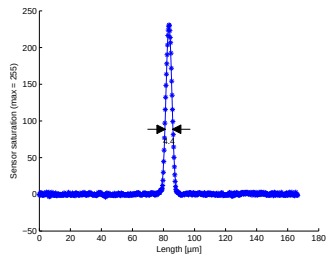

(c) A plot of the mode profile guided in the core.. The FWHM of the mode is approximated to 4.4 μm and is shown with black arrows.

Figure 3.2: Above are two images used to calculate the effective mode area of the two-hole fiber.

3.2.2 Filling the two-hole fibers

The holes of the two-hole fiber cover 1018 μm^2 each, giving a volume of 1018×L μm^2 where L is the length of the fiber. With a fiber length of 5 cm the volume required to fill the holes will be $2\times1018\times\text{L}\ \mu\text{m}^2 = 2\times1018\times5\times10^{-14}\ \text{m}^3 = 1.018\times10^{-7}\ \text{dm}^3 = 0.1018\ \mu\text{L}$. For each 5 cm of fiber the minimum amount of solution used, excluded any spillage due to leakage through the other end of the fiber, will be 0.1018 μL.

The fiber was filled by inserting it through a membrane-integrated lid and applying pressure inside the container with the solution. Figure 3.3 is a schematic drawing of how the fiber was inserted through the lid's membrane via a syringe needle. After removing the needle and making sure the fiber-end is below the surface of the solution, pressure was applied inside the container using a syringe filled with air. The time acquired to fill the fiber depends on the viscosity of the solution.

Using the pressure based method for filling the two-hole fibers with CNT, a

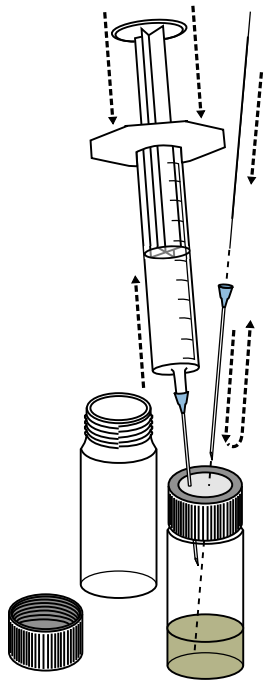

Figure 3.3: The procedure of filling hollowed fibers is shown in this figure. The container had a lid containing a membrane which the fiber needs to go through. Using a syringe needle the fiber was inserted through and then removed, with the tip of the fiber under the solutions surface. Afterwards air was pumped into the container through the membrane increasing pressure in the containers.

preliminary study was performed which did not give conclusive results. The most probable cause was due to insufficient modulation. In order to easier obtain a measurable modulation it is suggested to either increase the CNT concentration, the interaction length of the fiber or during fabrication reduce the hole to core distance. Since materials where limited for an in-depth investigation and no possibilities to fabricate custom designed fibers were available, a different sample design was necessary. Therefore a simpler design was suggested in order to evaluate the reliability of the setup. From this point the HI 1060 fiber was suggested and a new method of CNT attachment was used which allowed for a direct pulse interaction with the CNTs on the fiber tip.

3.2.3 HI 1060 commercial fiber

The HI 1060 fiber is a SM fiber used in this project in order to evaluate the concept of the measurement setup by direct light interaction with CNTs as saturable absorbers. If direct contact with the CNTs will not show any SA, then the much

weaker interaction with the evanescent field in the two-hole fibers will definitely not show any effects.

Table 3.2: Some parameters of the SM fiber HI1060 which have been used as reference fiber and concept testing. All data has been taken from the thorlabs webpage [24].

Operating Wavelength	> 980 nm
Cladding Outer Diameter	125 ± 0.5 μm
Coating Outer Diameter	245 ± 10 μm
Core Diameter	5.3 μm
Effective Mode area	30.2 μm^2

3.2.4 Deposition of carbon nanotubes on the fiber-end

The deposition of CNTs on the fiber-end was achieved by guiding light through a fiber while submerging the end into a CNT solution [25]. Although not conclusively verified, this method seems to be working due to thermophoresis from heating by optical absorption, helping the CNTs attach to the surface of the fiber-end.

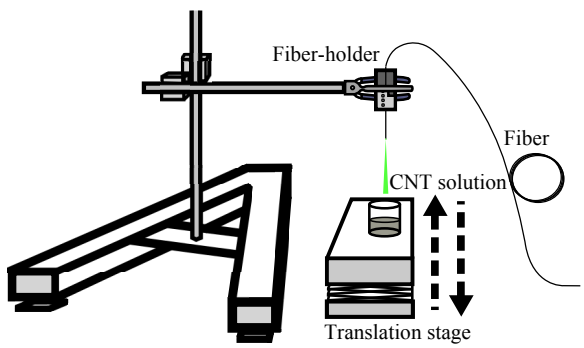

Figure 3.4: Illustrating the setup for depositioning CNTs on a fiber-end using guided light from a 532 nm laser.

Shown in figure 3.4, a translation stage was used in order to submerge the fiber-end into a DCB dispersed CNT solution while the fiber guided light of 532 nm, with output power from the fiber measured to be $\sim$35 mW. A laser with 14 mW at 633 nm output was also tested but was unsuccessful in showing signs of any CNTs being attached. After the desired time had passed, the laser was turned off and the translation stage slowly lowered, separating the solution from the fiber. A photo of the fiber being submerged in the CNT solution is shown in figure 3.5.

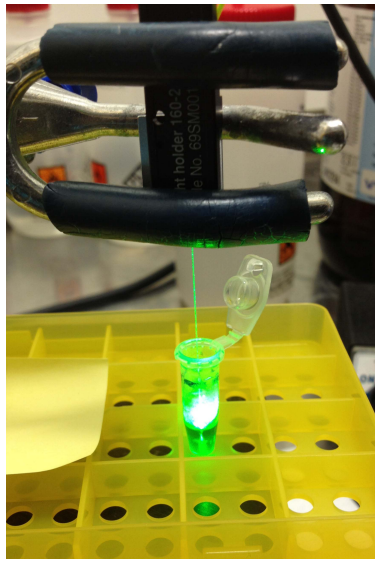

Figure 3.5: A photograph of the fiber submerged in the CNT solution.

The deposition method was investigated using several different fibers and set to guide light at different time periods and powers in the CNT solution. The fibers processed along with their parameters are shown in the table 3.3.

Table 3.3: Table of how the fibers were processed with CNT deposition. Some have been through additional processing after the normal procedure of CNT deposition, i.e Geen laser 4.

Label	P [mW]	t [minutes]	λ [nm]	Notes
Red laser 1	∼14	17	633	No change in transmission
Red laser 2	∼13	6	633	No change in transmission
Green laser 4	∼35	5/8/10	532	Processed, measured & cleaved 3x
Green laser 5	∼35	8	532	Confirmed CNT on fiber-end.
Green laser 6	∼35	8	532	Confirmed CNT on fiber-end
Green laser 7	∼35	3	532	Confirmed CNT on fiber-end
Green laser 8	∼35	12	532	Confirmed CNT, lower CNT conc.
Green laser 11	∼24	2	532	Confirmed CNT, lower CNT conc.

The fiber-end-surfaces were confirmed to have attached some CNTs by investigating them in a microscope (figure 3.6) and the transmission was compared with the measurements results of an optical spectrum analyzer (OSA).

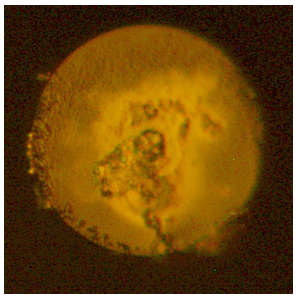

(a) The fiber-end of fiber labeled Green laser 1 with CNT visible on its surface after being processed for 5 minutes with ∼35 mW.

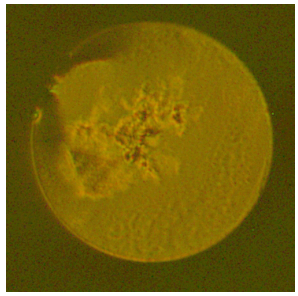

(b) The end-surface of a fiber after being processed for 8 minutes with ∼30 mW. Unfortunately the sample was accidentally damaged and was never used.

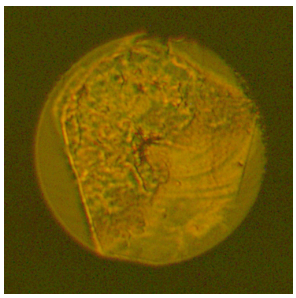

(c) Showing the fiber-end of Green laser 5 with CNT visible on its surface after being processed for 8 minutes with ∼35 mW.

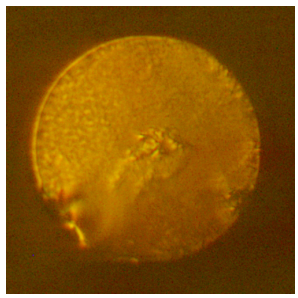

(d) Fiber labeled Green laser 6 with CNT visible on its surface after being processed for 3 minutes with ∼35 mW.

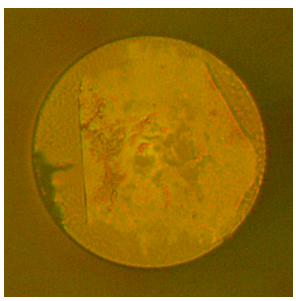

(e) Green laser 7:s fiber-end with CNT visible on its surface after being processed for 3 minutes with ∼35 mW.

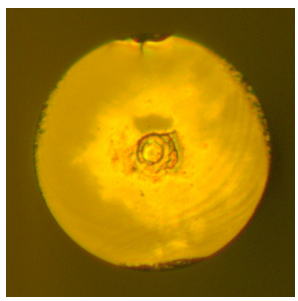

(f) The end-surface of fiber labeled green laser 8 with CNT visible on its surface after being processed for 12 minutes with ∼35 mW.

Figure 3.6: Here the fiber-end surfaces are shown looking through a microscope in order to visually confirm the attachment. The fiber type used for the CNT deposition was HI 1060 [24].

3.2.5 HI 1060 CNT deposition.

The white light source used for the OSA measurements as seen in figure 3.7 was a halogen lamp, which was focused using a lens and a microscope objective, into a MM fiber with the help of 3-D translation stages. With the MM fiber on the left and the CNT covered fiber to the right, the fiber-ends were brought up close to each other with the help of a fusion splicing apparatus (shown as the box in the figure) with high precision mechanic translation stages holding the two fiber. Due to the fine steps of the stages, which ensured reliable and repeatable input coupling, the free space coupling was optimized with the help of the fusion splicers two integrated cameras overlooking the fiber-ends from two angles and monitoring the output of the sample.

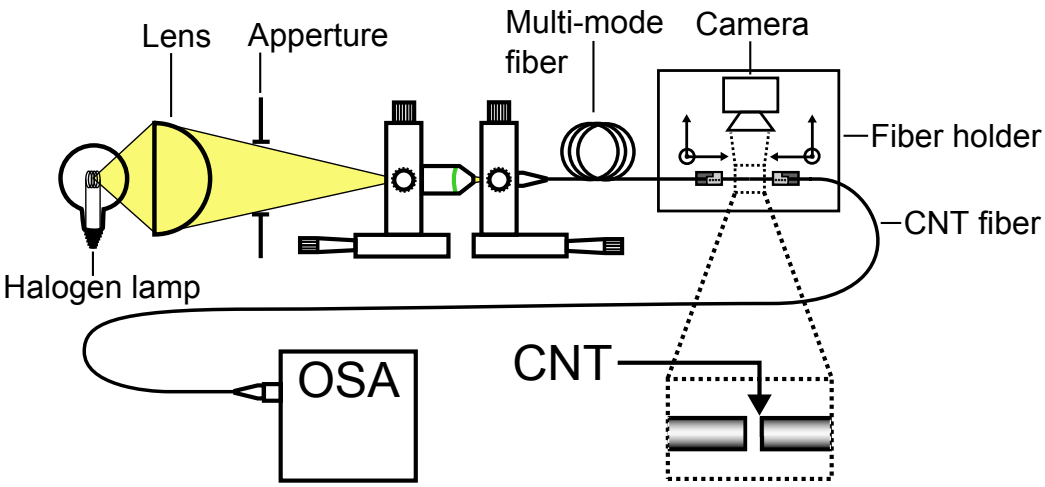

Figure 3.7: This figure depicts the setup used for guiding the white source from a halogen lamp for measurements with the OSA on the CNT covered HI1060 fibers. The results are shown in figure 3.8 for different CNT covered fibers.

The plot in figure 3.8 depict the Green laser 4 fiber whose ends have been covered by CNTs by submerging the fibers while guiding a source of 532 nm with $\sim$ 35 mW power for different periods of time. Shown in figure 3.8 starting from the top to the bottom are spectra from a clean reference, continuing with fibers that have been submerged for 5, 8 and 10 minutes.

An appropriate time for the deposition can be concluded to be 5 minutes or less in order to reduce scattering losses for this particular case. An extensive investigation could be performed to optimize the positioning time with respect to the CNT concentration, but due to lack of time and access to lab equipment, the work continued after two samples were fabricated. These two fibers are the Green laser 7 and Green laser 8 from table 3.3 where the CNT concentration of the solution for Green laser 7 was approximately doubled compared to Green laser 8

by drying the CNT solution to half its volume. Therefore the time parameters for Green laser 7 and 8 where 3 minutes and 12 minutes respectively.

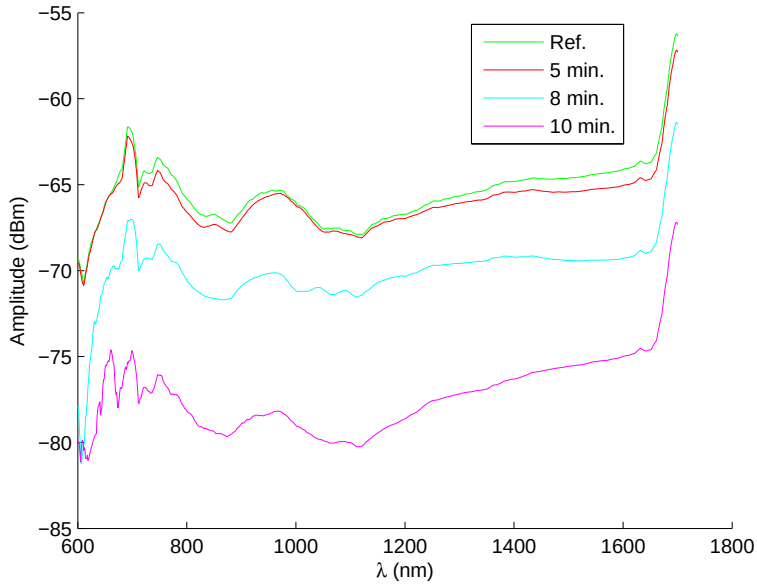

Figure 3.8: The graph shows the optical spectra of a HI 1060 fiber which has been end dipped into a CNT solution while guiding light from a ∼35 mW 532 nm laser during different time periods. Starting from the top the curves are green, red, magenta and purple. In this order they represent a measurement of a clean reference fiber, a fiber being dipped in the CNT solution with light guided for 5, 8 and 10 minutes. This particular fiber sample was called Green Laser 4 seen in table 3.3.

3.3 Characterization setup

The characterization setup was designed to conduct transmission measurements of short fibers, around 5-10 cm, by comparing the change of the input with the output amplitude from the fiber. These power measurements where performed utilizing a single diode with a chopper to separate the input and output signals of the fiber, with an Origami laser used as source.

Seen in figure 3.9 is an overview of the fiber transmission measurement setup where the source is labeled as the Origami laser. Some of the source's parameters have been shown in table 3.4.

The setup overview can be divided into three segments, the beam path from the Origami laser up to the fiber enclosing box, the signal redirected from the fiber

box to the diode and the path propagating through the fiber and then reflected to the diode.

3.3.1 Setup overview

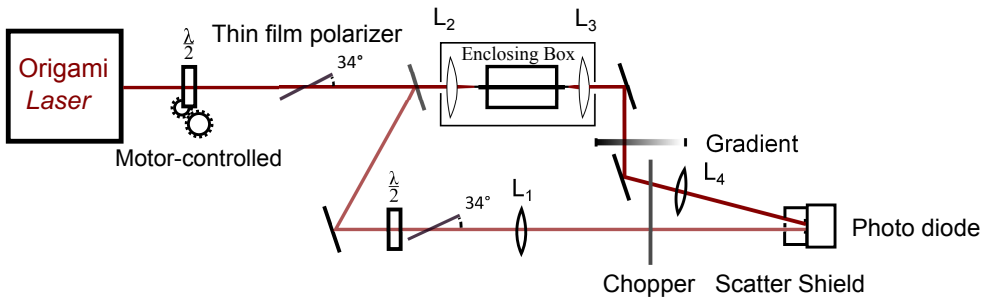

Figure 3.9: A simplified overview of the measurement setup used for collecting the power data of the transmission through the substrate.

Starting with the point from the Origami laser, figure 3.9 shows the beam going through an attenuator consisting of a computer controlled motorized rotator with a lambda half-plate attached and a thin film polarizer at Brewster angle. Due to the horizontal polarization of the laser output, the thin film polarizer set at Brewster angle will reflect vertical and transmit horizontal polarizations as shown in figure 3.10. The lambda half-plate and thin film polarizer will therefore attenuate the horizontally polarized beam output of the Origami laser by rotating the lambda half-plate, changing the polarization angle before the thin film polarizer.

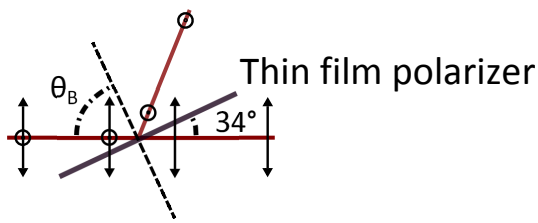

Figure 3.10: Looking from above at a vertical and horizontal polarized beam, the thin film polarizer at Brewster angle will reflect the vertical positioned polarization and transmit the horizontal.

After passing through the variable attenuator the beam will reach a mirror reflecting $\sim 1\%$ and transmitting the rest of the signal into the enclosed box.

Following the $\sim 1\%$ reflected signal, it will get though another attenuator with the same components as previously discussed except for a fixed lambda half-plate. The signal continues through a lens L_1 with focal length of f = 300 mm and passes

a chopper set at 85 Hz with 50 % duty cycle, to focus on the diode sensor. The attenuation of the $\sim 1\%$ reflected signal was required because at this point it still managed to saturate the diode at maximum power.

Resuming the path from the point the transmitted signal enters the enclosed box, the beam will get focused through lens L_2 with focal length 20 mm. L_2 is fixed but the fiber holder can be moved in the three spacial directions, along the propagation axis, along the sides and the height, in order to set the focus on the fiber core. After the fiber, lens L_3 with focal length $f = 8$ mm and free axial movement in the propagation axis is set in order to focus the output signal. Reflecting the output beam through a neutral density gradient filter, the output is reflected through the chopper and then focused on the diode sensor with L_4 with focal length 150 mm. The diode itself has a cover with two holes to shield from most of scattered light.

The advantage of this setup is that it only utilizes one diode and therefore the diode response will be the same for both the input and output signals and can therefore be excluded when comparing the two. The input and output signals were set at different chopper frequencies in order to separate the signals from each other. The attenuation of both signals were also set to have the same amplitude when measuring the diode signal. The absolute maximum power measurements were therefore done in advance and used as a calibration function, which will be discussed later in this chapter.

3.3.2 Introspection of the measurement attained

With the chopper blocking one of the signals at the time, both the input and output signal could be measured and saved using the oscilloscope connected with the diode with 8-bits resolution. Each measurement would result in one data point for the input and output signal of the fiber. With each measurement, the output beam of the Origami laser would be attenuated by changing the angle of the lambda half-plate on the motorized rotator, changing the horizontal polarization towards the vertical polarization. An example of one measurement point is shown in figure 3.11 where the chopper separates the input and output signal. In the plot there are flat zones, one peak and a dip in a recurring pattern. Starting from the left, the flat zones corresponds to the output signal on the first flat zone, the background noise where the dip is formed due to none of the signals reaching the diode sensor, the next flat zone is the input signal, then the peak where both signals reach the sensor and in some cases saturate it. After the peak the pattern repeats with the output signal.

This measurement is done with each attenuated point of the output beam from the laser, where each input and output signal zone average will result to be the signal at that particular attenuation point given in the units of volt. With this a measurement sweep can be done where the lambda half-plate is rotated from angle $\theta = 0^\circ$ to $\theta = 45^\circ$ with steps of one degree, slowly attenuating the output beam via the thin film polarizer set at Brewster angle. The outcome of one complete

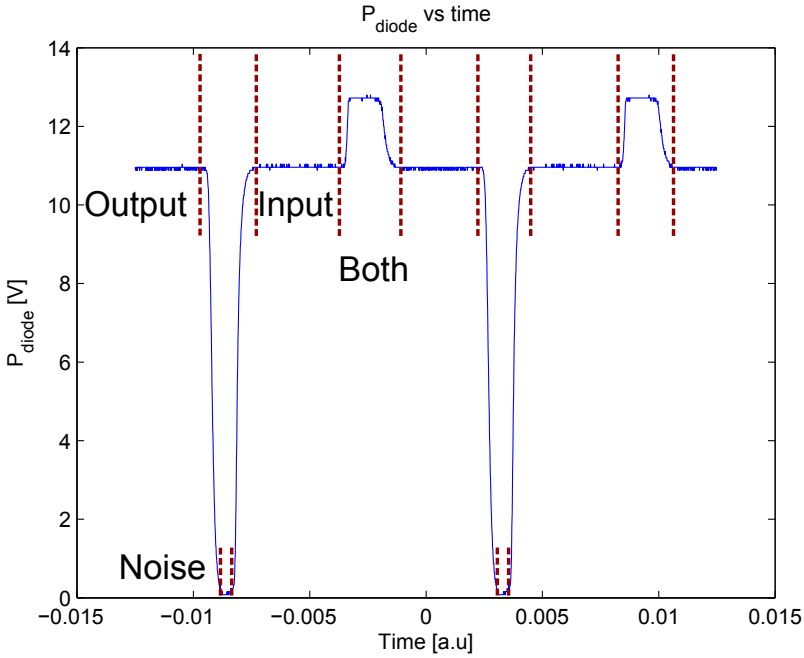

Figure 3.11: The signal from the diode to the oscilloscope (with 1 MΩ input impedance) showing the voltage vs an arbitrary time. This plot contains both the output signal of the fiber and input beam before the fiber. The dips show the background noise and the higher both the the output and input signals, in this case saturating the diode. The attenuation was at an angle where the beam had the highest transmission.

measurement sweep is shown in below in figure 3.12, where the lambda half-plate angles lies between $136° \leq \theta \leq 181°$.

As seen and described in figure 3.9 only a single diode was used in this setup, where the distinction of both signals was achieved using a chopper. Since each diode can have slightly different proportionality of diode signal depending on the incoming intensity or due to nonlinear responses, any slight variation will be removed if both the fiber input and output beam are attenuated to show a similar intensity level when reaching the diode. The remaining major problem was slightly unstable input coupling into the fiber core due to either pointing instability of the laser output or vibration-induced instability of the employed optomechanics, for example the fiber holder on the translation stage shifted a few to hundreds of micrometers over time. In order to reduce the beam walking effect a large quantity of fast measurements were performed to see if the deviation between the two is to big. The shift in the translation stage forced a stop and realignment of the fiber in order to continue the

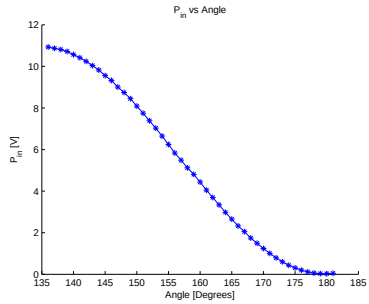

(a) The averaged input signal from the diode (see fig. 3.11) plotted against the angle of the motorized rotator holding the $\lambda/2$-plate for attenuating the laser output.

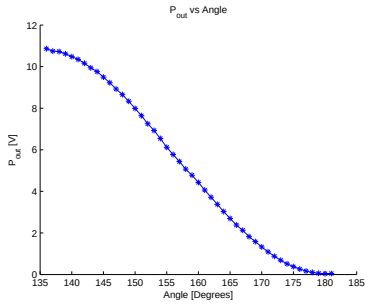

(b) Similar to fig. 3.12a the output signal was plotted against the attenuation angle.

Figure 3.12: The corresponding signals amplitudes from fig. 3.11 have been averaged and plotted as a function on how much the attenuating lambda half-plate from the laser output beam in figure 3.9 has been rotated. The whole attenuation span is $136° \leq \theta \leq 181°$.

measurements. Therefore, a quick measurement routine was necessary to gather as much data as possible, while eliminating the effects from detrimental instabilities.

In figure 3.13 the input power is shown as a function of the rotation angle of the variable attenuator. The blue circles show how a complete rotation of the lambda half-plate will attenuate the beam, while the red dots depicts the attenuation region chosen for the measurements (see figure 3.12), between 136° and 181°. Due to damage on the lambda half-plate, the first and third peaks are deformed and therefore the attenuation region chosen was after the second peak. The black line is a sine curve fit.

The dynamic range of the red dotted curve is 108 dB, but due to noise causing disturbance at lower intensities, measurements were performed between 136° and 170° resulting in a dynamic range of 44 dB.

3.3.3 Input coupling efficiency

The pulses from the probe laser were sent into the fiber using free space incoupling, focusing into the core through a lens. Since the fiber core radius usually is a few μm in dimension, any slight deviation in the beam path or movement of the fiber will noticeably affect the incoupling.

Two examples of incoupling are shown in figure 3.14 for two different HI 1060 end dipped samples from table 3.3. As seen in 3.14a the cladding is clearly visible with a close to homogeneous distribution of light (except from the CNTs shadows)

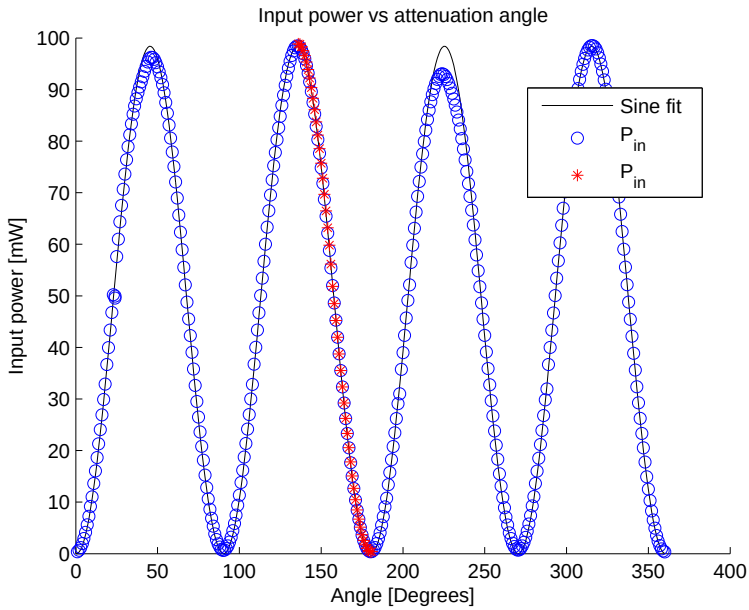

Figure 3.13: The variable attenuator was rotated from 0° to 360° and the power measured using a power meter. Shown is the result of the measurement (blue), a sine curve fit (black) and the range that was used for the characterization measurements (red).

with no attenuation of the incoupled beam, while in 3.14b the core shines bright and saturates the pixels of the camera, even though the beam has been attenuated.

In order to ensure that the input coupling of the laser into the fiber was optimized, a camera (in order to see the end-surface) and a power meter (to measure the output power) were placed after the fiber. When the fiber input coupling is optimized the power meter should show the most amount of power being guided through the fiber and the camera show the core as a bright spot with a dark cladding. The better the input coupling into the core the darker the cladding appears with respect to the core.

3.4 Probe pulses

The pulse length was monitored throughout the measurement setup by using an autocorrelator and a commercial laser source. First will the laser source and its parameters will be discussed followed by measurements of the pulse width.

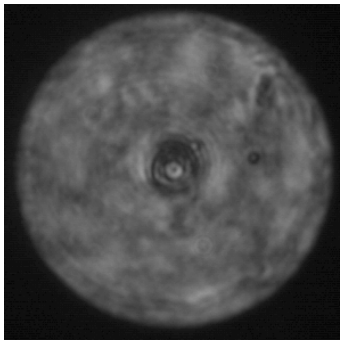

(a) Example of a bad incoupling for a CNT surface covered fiber (Green laser 11 in table 3.3).

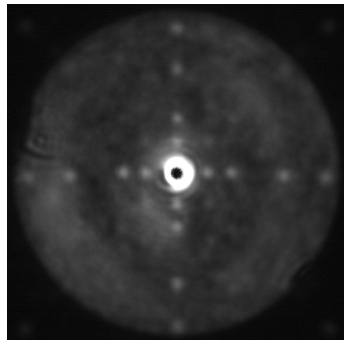

(b) An example of good incoupling for another CNT covered fiber (Green laser 7 from table 3.3).

Figure 3.14: Two examples are shown for bad and good incoupling of two different HI 1060 CNT end-surface covered fibers.

3.4.1 Origami Laser

The laser source for the characterization measurements was the Origami laser and can be seen in figure 3.9 and 3.17 as a box with the name Origami laser. This laser is a commercial laser from the company OneFive [26].

The maximum output power of the laser is 100 mW, but due to losses through a variable attenuator and other optical elements, the maximum power coupled into the fiber was in the range of ∼98 mW (as shown in figure 3.12a). Using these powers, the calculated maximum pulse energy E_{pulse} is shown in equation (3.1), where the measured beam power P_{beam} along with both the specified maximum repetition rate f_{rep} and the measured repetition rate (figure 3.15a) have been used.

$$E_{\text{pulse}} = \frac{P_{\text{beam}}}{f_{\text{rep}}} = \frac{98 \text{ mW}}{40 \text{ MHz}} = 2.45 \text{ nJ}, \tag{3.1}$$

The repetition rate was measured with a radio frequency analyzer (RFA) resulting in 40 MHz. The first harmonic of the Origami lasers repetition rate along with the frequency comb showing the first, up to the tenth harmonic are shown in figure 3.15.

The spectrum of the laser is shown in figure 3.16 where the peak center is at 1046 nm with a FWHM bandwidth of 7.5 nm.

Finally a tabular with calculated and specified parameters are shown in table 3.4.

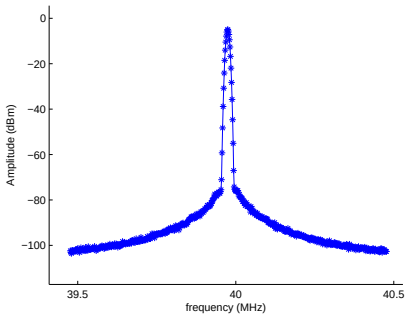

(a) The fundamental repetition rate of the Origami laser with resolution bandwidth (RBW) of 9.1 kHz.

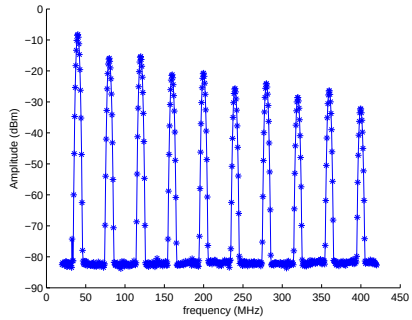

(b) The frequency comb measured with a RFA with RBW of 3.0 MHz, where the fundamental repetition rate is 40 MHz and the higher harmonics shown.

Figure 3.15: Above shows the RFA measurements conducted on the probe laser.

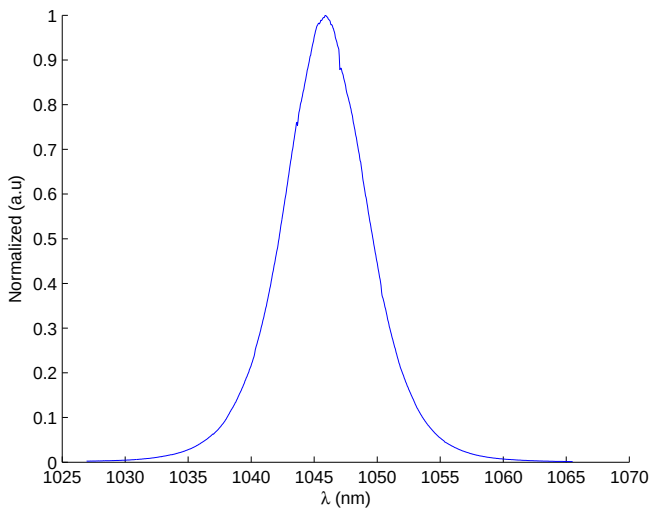

Figure 3.16: The spectra of the Origami laser, measured with a RBW of 0.06 nm, with its peak center at 1046 nm and bandwidth of 7.5 nm.

Table 3.4: Some parameters of the Origami-10 laser from the company OneFive, showing parameters either measured or calculated.

λ_0	1046 nm
τ_p	$\sim$ 160 fs
f_{rep}	40 MHz
E_{p}	2.45 nJ
Polarization output	Horizontal

3.4.2 Non-collinear interferometric autocorrelator

Pulses of femtosecond widths can only be measured with a few selected methods where one is the autocorrelator, which utilizes an optical systems with either interferometric (collinear) or background-free (non-collinear) autocorrelation. The method used was the background-free autocorrelation, where the incoming beam gets split into two parts with a controllable small delay added to one of the beams. By superimposing the two beams on each other in a nonlinear χ^2 crystal, a frequency sum signal will be generated which will depend on the level of overlap between the two pulses. Only when the beams coincide at the right angle inside the crystal will there be second harmonic generation. As a result the sum frequency generated signal will be the convolution of the incoming pulses.

After acquiring the convolution width the result can be used to calculate the real pulse width. In this project a commercial autocorrelator was used from Spectra-Physics[1].

3.4.2.1 Pulse width measurements

The setup for measuring the pulse width of the input and output of a $\sim$5 cm long fiber is show in figure 3.17. All mirrors are metallic mirrors and the lenses have an anti-reflection (AR) coating covering 650-1050 nm. Due to the lack of power control of the Origami laser the output is led to an attenuator in order to decrease the power. In order to measure the laser pulse FWHM the beam was first led to the autocorrelator using mirrors as shown with the dashed lines in figure 3.17. Thereafter the mirrors were removed and the fiber output was measured.

3.4.2.2 Calculating the pulse width

The signal shown from the autocorrelator is the convolution of the incoming pulses. That signal will therefore vary depending on the original pulse shape. Due to the convolution the signal will always be symmetrical when the autocorrelator is properly aligned.

A measurement example can be seen in figure 3.18 where the curve fit of the autocorrelator pulse is shown. In order to get the real time scale in figure 3.18, the

[1]Spectra-Physics, Autocorrelator Model 409-08

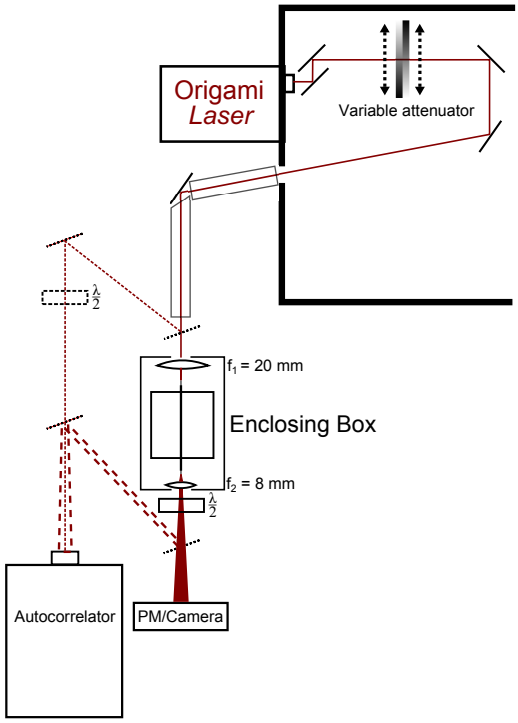

Figure 3.17: The overview of the measurement setup used for measuring the FWHM of the incoming pulses. Only one of the dashed paths could be measured at the time, one before the fiber setup (the enclosing box) and one after the beam had gone through the fiber.

pulse had been delayed in time by introducing an etalon into the optical pathway. Because this shift is known, the time scale can be calculated from the length of the shift.

After the measurement, the data must get processed with two simple steps in order to get the real width of the pulse. First the pulse duration must get acquired and then multiplied with a deconvolution factor depending on what the original pulse shape was. For Gaussian pulses the deconvolution factor is 0.707 and 0.647 for sech^2 pulses. With the Origami lasers sech^2 shaped pulses the resulting pulse widths for both the input and output of the fiber resulted in $\tau_{p_{in}} = 158$ fs and $\tau_{p_{out}} = 201$ fs.

3.4.3 Calculating the dispersion and nonlinear lengths

With the theory of dispersion and SPM been discussed in section 2.1.1 and the dispersive and nonlinear regime in section 2.1.2, it is of interest to use this knowledge

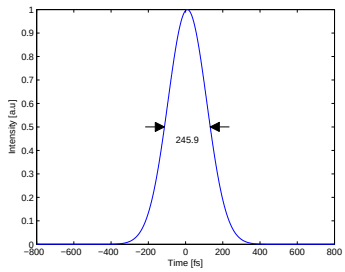

(a) The curve shows the autocorrelator pulse width before propagating through the fiber (see figure 3.17), giving the input signal pulse duration.

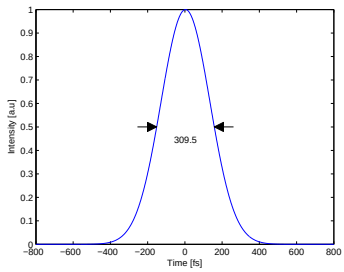

(b) Similar to figure 3.18a the autocorrelator measurement after propagating through the fiber, showing the output signal pulse duration.

Figure 3.18: The input and output pulses of the fiber shown from the autocorrelator and therefore the pulse duration shown in the graph still has to be converted with the deconvolution factor in order to show the pulse duration of the laser.

in order to calculate what effects have the greatest influence for pulse propagation in the commercial HI 1060 fiber samples.

3.4.3.1 The dispersion length

In order to calculate the dispersion length and nonlinear length a couple of parameters must be determined. For equation (2.18) the initial pulse width and the GVD parameter must be determined. The initial pulse width was measured to be $\tau_p = 158$ fs after converting the FWHM in figure 3.18a. The GVD parameter can be calculated from equation (2.9) if the dispersion coefficient is obtained for fused silica giving

$$\beta_2 = -\frac{2\pi c}{D\lambda^2} \approx 18.2 \text{ ps}^2/\text{km}, \tag{3.2}$$

where the wavelength was 1046 nm and the dispersion coefficient was taken from a diagram in Agrawal [27] shown in figure 3.19 , which was approximated to -31.5 ps/km nm. Using equation (2.18) for the dispersion length, equation (2.14) for the pulse width $\mathrm{T}_0 = 263$ fs and the GVD parameter from equation (3.2), results in

$$\mathrm{L}_D = \frac{\mathrm{T}_0^2}{|\beta_2|} = 3.8 \text{ m} \tag{3.3}$$

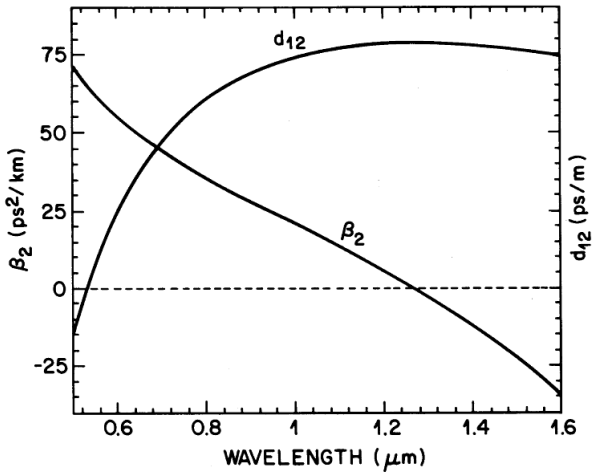

Figure 3.19: The wavelength dependence is displayed for the dispersion coefficient β_2 and walk-off parameter d_{12} [27].

Comparing the fiber length L (which ranges between 5 - 6 cm) to the dispersion length L_D shows $L \ll L_D$ suggesting low dispersive effects from the fiber on the pulses.

3.4.3.2 The nonlinear length

In order to get some sense of the nonlinear length, the nonlinear coefficient γ and peak power P_0 must be calculated. Starting with the nonlinear coefficient, equation (2.12) shows the need for the nonlinear refractive index at wavelength 1046 nm and the effective mode area in order to calculate γ. Acquiring the effective mode area $A_{eff} = 30.2\ \mu m^2$ from table **??** for HI 1060 fibers and the nonlinear refractive index for fused silica, $n_2 = 2.75 \times 10^{-20}\ m^2/W$ from Miliam [28] at wavelength 1.06 μm (which will not deviate much from the refractive index at wavelength 1046 nm), the nonlinear parameter becomes

$$\gamma = \frac{n_2\omega_0}{c\pi w^2} = \frac{n_2\omega_0}{cA_{eff}} \approx 5.47\ W^{-1}\ km^{-1}.$$

The last term to determine in (2.19) is the peak power P_0 which is composed of the pulse energy E_p, the pulse duration τ_p and a constant factor depending on the pulse shape. For Gaussian pulses the factor is ≈ 0.94 and for $sech^2$ its ≈ 0.88.

$$\begin{aligned} P_0 &\approx 0.94\frac{E_p}{\tau_p} \qquad \{\text{Gaussian pulse}\} \\ P_0 &\approx 0.88\frac{E_p}{\tau_p} \qquad \{\text{sech}^2 \text{ pulse}\} \end{aligned} \tag{3.4}$$

With $E_p = 2.45$ nJ and $\tau_p = 158$ fs the peak power for a sech^2 pulse is $P_0 = 13.6$ kW.

With this case in mind the nonlinear length from equation (2.19) becomes

$$\begin{aligned} &\mathrm{L}_{NL} \approx 1.34 \text{ cm}, \\ &\text{for sech}^2 \text{ pulses.} \end{aligned} \tag{3.5}$$

Comparing the fiber length with the nonlinear length shows that $\mathrm{L} \gtrsim \mathrm{L}_{NL}$ which suggests SPM effects should be evident. This means that equation (2.26) holds true and with a positive β_2, the case of normal dispersion applies.

Seeing the calculated dispersion length $\mathrm{L}_D = 3.8$ m and the nonlinear length $\mathrm{L}_{NL} = 0.68$ cm and comparing to the typical fiber sample length of $\mathrm{L} = 5$ cm, suggests that the pulse will get new spectral components with spectral broadening. The most dominant effect is from SPM due to the nonlinear length being smaller than the fiber length while the dispersion length is some magnitudes larger. But the pulse can still be broadened due to new frequency component generation from the SPM effect, creating new components that may receive greater influence from dispersion. Comparing the resulting pulse width before the fiber of $\tau_{p_{in}} = 158$ fs and the width after the fiber of $\tau_{p_{out}} = 201$ fs shows that there is some pulse broadening, with same magnitude as examined with a pulse propagation simulation for a passive fiber.

Chapter 4

Experimental results

In the previous chapter the measurement setup was explained in detail along with the sample preparation. Before discussing the results of the measurements, a brief explanation of the measurements will be given.

There were several substrates fabricated were CNTs were attached on the end-surface of commercial fibers from Thorlabs called HI 1060 [24], in order to let the coupled light directly affect the CNTs. For more details on these fibers and the preparations see section 3.2.

4.1 HI 1060 fiber measurement results

After attaching the CNTs on the HI 1060 fiber's end-surface and visually observe them in a microscope (see figure 3.6), the sample was measured using an OSA with the setup seen in 3.7 with the results given in figure 3.8.

4.1.1 Nonlinear transmission results

Using the characterization measurement method discussed in the previous chapter, measurements were performed on a CNT covered fiber. The characterization was done in two steps, first a measurement of a reference fiber which lacked any CNTs was conducted followed by a second measurement of the sample fiber with CNTs. These two measurements where processed in order to get their transmissions and then compared by dividing the transmission of the fiber sample with the reference.

The output and input signal attained from the diode (see figure 3.12) are called $V_{\text{out}}(\theta)$ respectively $V_{\text{in}}(\theta)$ where each of them are dependent on the lambda half-plate angle θ. Before the measurement sweep was started, the maximum output from the fiber $P_{\text{out}_{\text{max}}}$, directly after lens L_3 in figure 3.9, was acquired with a power meter in order to relate the diode's maximal signal (which was set to always show 11 V at the maximum) to the real power amplitude. The output and input signal angle dependence can therefore be changed into power, giving $V_{\text{in}}(P_{\text{in}})$ and

$V_{\text{out}}(P_{\text{in}})$, where P_{in} is the power of the attenuated laser beam with its maximum power at $P_{\text{in}_{\text{max}}}$.

The signals were converted to show the fluence in equation (4.1)

$$\begin{aligned} F_{\text{out}}(P_{\text{in}}) &= \frac{V_{\text{out}}(P_{\text{in}})}{V_{\text{out}}(P_{\text{in}_{\text{max}}})}\frac{P_{\text{out}_{\text{max}}}}{A_{\text{eff}}f_{\text{rep}}} = \frac{V_{\text{out}}(P_{\text{in}})}{V_{\text{out}}(P_{\text{in}_{\text{max}}})}\frac{E_{\text{out}_p}}{A_{\text{eff}}}, \\ F_{\text{in}}(P_{\text{in}}) &= \frac{V_{\text{in}}(P_{\text{in}})}{V_{\text{in}}(P_{\text{in}_{\text{max}}})}\frac{P_{\text{in}_{\text{max}}}}{A_{\text{eff}}f_{\text{rep}}} = \frac{V_{\text{in}}(P_{\text{in}})}{V_{\text{in}}(P_{\text{in}_{\text{max}}})}\frac{E_p}{A_{\text{eff}}}, \end{aligned} \tag{4.1}$$

where A_{eff} is the effective mode area of the fiber, f_{rep} is the repetition rate of the laser and $E_{p_{\text{out}}}$ and E_p are the pulse energies for the output and input signals from the fiber. The same was done with the reference signals giving

$$\begin{aligned} F_{\text{out}_{\text{ref}}}(P_{\text{in}}) &= \frac{V_{\text{out}_{\text{ref}}}(P_{\text{in}})}{V_{\text{out}_{\text{ref}}}(P_{\text{in}_{\text{max}}})}\frac{P_{\text{out}_{\text{ref}_{\text{max}}}}}{A_{\text{eff}}f_{\text{rep}}} = \frac{V_{\text{out}_{\text{ref}}}(P_{\text{in}})}{V_{\text{out}_{\text{ref}}}(P_{\text{in}_{\text{max}}})}\frac{E_{\text{out}_{p_{\text{ref}}}}}{A_{\text{eff}}} \\ F_{\text{in}_{\text{ref}}}(P_{\text{in}}) &= \frac{V_{\text{in}_{\text{ref}}}(P_{\text{in}})}{V_{\text{in}_{\text{ref}}}(P_{\text{in}_{\text{max}}})}\frac{P_{\text{in}_{\text{max}}}}{A_{\text{eff}}f_{\text{rep}}} = \frac{V_{\text{in}_{\text{ref}}}(P_{\text{in}})}{V_{\text{in}}(P_{\text{in}_{\text{max}}})}\frac{E_p}{A_{\text{eff}}}. \end{aligned} \tag{4.2}$$

The transmission ratio of the output and input signals was acquired for both the reference and sample fiber with the help of equation (4.3), where the power dependence was substituted with the output fluence with the help of figure 3.12 and $F = \frac{P}{A_{eff}f_{\text{rep}}}$.

$$\left.\begin{aligned} T(P_{\text{in}}) &= \frac{F_{\text{out}}(P_{\text{in}})}{F_{\text{in}}(P_{\text{in}})} \\ T_{\text{ref}}(P_{\text{in}}) &= \frac{F_{\text{out}_{\text{ref}}}(P_{\text{in}})}{F_{\text{in}_{\text{ref}}}(P_{\text{in}})} \end{aligned}\right\} \Rightarrow \frac{T(P_{\text{in}})}{T_{\text{ref}}(P_{\text{in}})} \Rightarrow \{\text{using figure 3.12}\} \Rightarrow \frac{T(F_{\text{out}})}{T_{\text{ref}}(F_{\text{out}})} \tag{4.3}$$

4.1.2 Characterization measurement results

The calibrated transmission data from equation (4.3) have been plotted in figure 4.1 and 4.2 for samples Green laser 7 and 8 in table 3.3, against respective reference fiber. Shown are two sets of a multitude of measurement sweeps conducted for each fiber sample shown as black circles in corresponding figure.

The increasing spread of measurement points for lower fluence levels are most probable due to input coupling fluctuations being more severe at lower powers, since the coupling was calibrated at the peak power. Also comparison between each measurement curve, small input coupling fluctuations may be present due to movement of the fiber holder or beam walking of the laser output, resulting in additional input coupling variations between the two measurement sets overlaid on both plots.

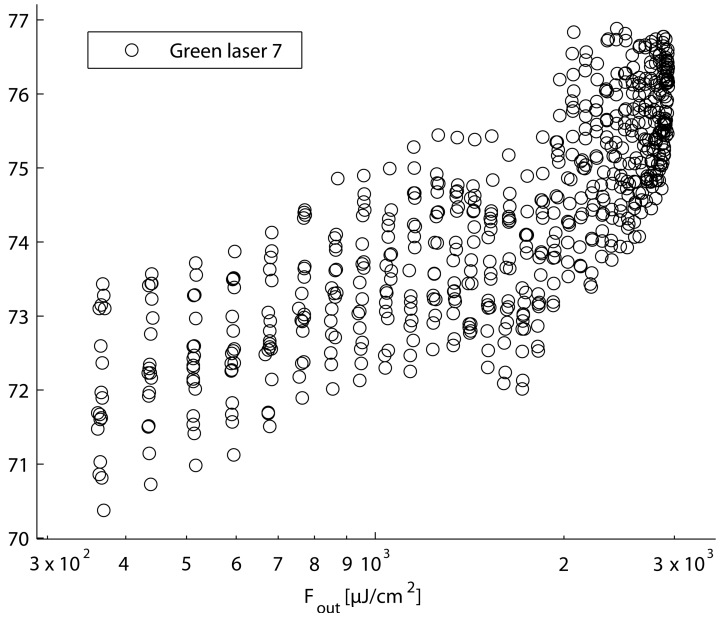

Figure 4.1: The transmission ratio between a CNT end-surface covered fiber and a reference fiber is plotted against the output fluence. The CNT fiber used was Green laser 7 from table 3.3.

In both plots there is a raise of transmission of the CNT fiber when the fluence reaches close to 2 mJ/cm^2 suggesting where the CNT saturable absorber starts to saturate. Although this is much larger than what was reported by [29] (10 μJ/cm^2) the difference can be probably explained with mainly figure 3.6f where the CNTs can be seen to have been attached mostly around the core mostly therefore only interacting with the evanescent field. Also the CNTs absorption wavelength dependence can be a smaller factor since 1046 nm was used in this project while 1.3 μm was the specified wavelength in the article [29].

In the span of the measurement, the transmission increased with 2% for Green laser 7 and 2.5% for Green laser 8. For both plots an increasing trend is visible as well as a sudden dip just before the 2 mJ/cm^2 fluence mark which is most probable due to the attenuator having some faulty in that specific area, composing of damage on the lambda-half plate that affects the beam path or polarization, or junk absorbing some of the laser output.

A fully saturated transmission measurement will have the shape of the nonlinear transmission function [30]

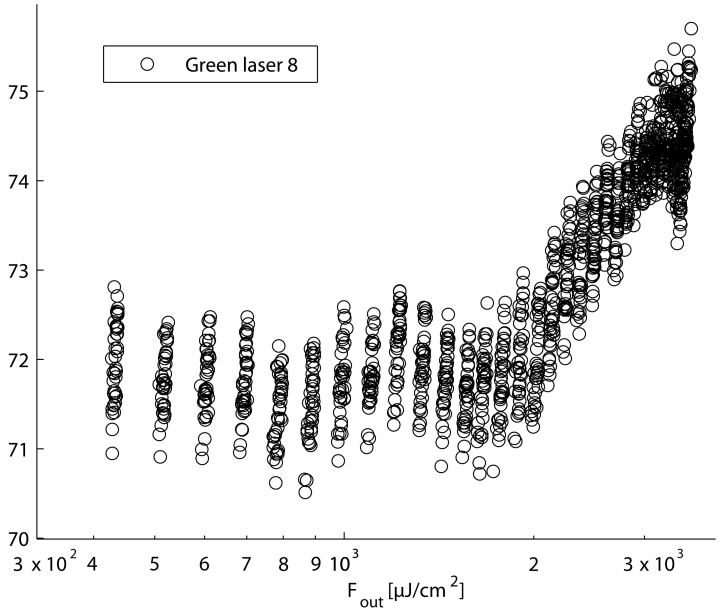

Figure 4.2: Same as in fig. 4.1 but done with a different end-surface CNT covered fiber (Green laser 8, see table 3.3).

$$T(F_{\text{out}}) = T_{\text{ns}} - \left(1 - \exp\left[-\frac{F_{\text{out}}}{F_{\text{sat}}}\right]\right)\frac{F_{\text{sat}}}{F_{\text{out}}}\Delta T, \tag{4.4}$$

with the non-saturable transmission T_{ns}, the saturation fluence F_{sat} and the fluence of the reference fiber output F_{out}. But since the saturation fluence is higher than the laser output, the SA samples never got saturated. Curve fitting with the nonlinear transmission function was therefore impossible due to the free parameters T_{ns} and ΔT, thus also rendering it impossible to find the saturation fluence F_{sat}.

The modulation depth in both plots are affected by ΔT which at most can only have a slight difference between the plots, with the observable ΔT appearing to be slightly larger in the later due to the small increase of the slope.

4.1.3 Long-term stability measurements

Since no active fixation of the CNTs was performed, the CNTs are expected to gradually fall of the fiber-end tip, therefore gradually degrading the nonlinear absorption properties of the prepared samples. Using the same fiber as in figure 4.2 the measurement was repeated two more times with a few days intervals. The

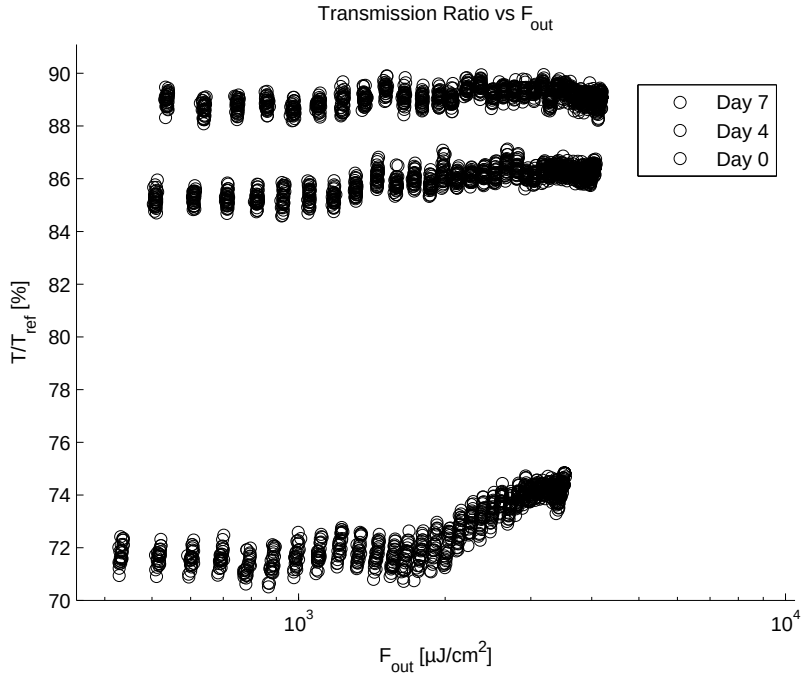

Figure 4.3: The measurement of Green laser 8 fiber from table 3.3 and figure 4.2 has been plotted along with two more repeated measurements done several days later. It seem the CNT slowly detach themselves from the fiber ends over time.

result is shown in figure 4.3 where the lowest curve is the first measurement done on the same day the fiber was fabricated, while the other measurements seem to flatten out and rise in transmission with passing time. Comparing with the first curve at day 0 with a transmission difference of 2.5%, the next curve showed a transmission difference of 1%, with the last curve not showing any distinct transmission differences. The characterization setup has therefore produced working results shown with this time degrading sample where the modulation depth decreases over time.

Chapter 5

Conclusion and outlook

A setup for characterization of fiber integrated CNTs has been realized and tested. This setup is shown to be reliable but the repeatability of the sample preparation must be improved. The results show a start of fluence saturation at 2 mJ/cm^2 with a transmission difference of 2.5% from the start to the end of the measurement. The transmission curve can be modeled with equation (4.4) [30], but due to low laser output effect complete saturation never occurs for the SA fiber samples. Comparing these results to the 10 $\mu J/cm^2$ which was achieved by [29] strongly suggest the CNTs are mainly gathering around the core, as can also be seen in figure 3.6f, allowing only the evanescent field of the guided light to interact with the saturable absorber.

With the CNTs being completely exposed to the environment, it was expected for them to detach themselves over time. This assumption was investigated and confirmed with the performance of three measurements conducted over the span of a week. With a transmission difference of 2.5%, the difference decreased down to 1% and became non-discernible with the setups resolution in the last measurement. The transmission base levels increased as well, from 72%, to 85% and 89% respectively. These are clear indications of a decreasing modulation depth, as well as absorption, over time which confirms both the presence of measurable CNTs on the fiber-end as well as the setups ability to conduct SA measurements. The detachment problem can be solved by either incorporating the CNTs into the fiber or by mixing them with a host material with low absorption.

Future measurement improvements can be realized with either higher laser outputs or increased field overlap with the CNTs. In order to achieve a more homogeneous distribution of CNTs, different deposition techniques can be tested. For instance an evaporation method by letting droplets evaporate from the fiber tip, gradually building up more layers with each succession. The prospect of this method can be a more homogeneous distribution but with the possibility of dissolving the previous layers when applying a new droplet.

Due to the lack of time and some problems with the probe laser occurring towards the end of the project, any detailed investigation on the 2-hole fiber

measurements and application of samples into a fiber mode-locking setup were not performed. By filling holed fibers with CNTs and letting the evanescent field interact with the CNTs, the maximum incorporation of CNTs can be achieved, which would probably result in a longer sample and interaction length in order to compensate for the main problem of weak nonlinear interaction. Conclusive tests need therefore to be performed in order to identify the parameter dependencies between CNT concentration and interaction length. The use of PMMA in the CNT solution can also be investigated. The evanescent interaction radial length from the core can also be investigated by either acquiring fibers with the hole positioned closer to the core or increasing the core radius, keeping in mind that the refractive index difference between cladding and core also needs to be changed in order to maintain SM operation (see equation (2.4)).

The next logical steps for future work based on the results of this project are the incorporation of the CNTs into the 2-hole fibers and integrating the samples into a fiber laser setup for mode-locking.

References

[1] N. M. A. 2013, "The nobel prize in physics 2010," February 2014. Available: http://www.nobelprize.org/nobel_prizes/physics/laureates/2010/.

[2] N. M. A. 2013, "The nobel prize in chemistry 1996," February 2014. Available: http://www.nobelprize.org/nobel_prizes/chemistry/laureates/1996/.

[3] S. Iijima, "Direct observation of the tetrahedral bonding in graphitized carbon black by high resolution electron microscopy," *J. Cryst. Growth*, vol. 50, pp. 675–683, 1980.

[4] S. Iijima, "Helical microtubules of graphitic carbon," *Nature*, vol. 354, pp. 56–58, November 1991.

[5] J. Clendenin, J.-W. Kim, and S. Tung, "An aligned carbon nanotube biosensor for dna detection," *NEMS 2nd IEEE Int. Conf.*, pp. 1028–1033, January 2007.

[6] K. S. Kim, Y. Zhao, H. Jang, S. Y. Lee, J. M. Kim, K. S. Kim, J.-H. Ahn, P. Kim, J.-Y. Choi, and B. H. Hong, "Large-scale pattern growth of graphene films for stretchable transparent electrodes," *Nature*, vol. 457, pp. 1028–1033, February 2009.

[7] C. Journet, W. K. Maser, P. Bernier, A. Loiseau, M. L. la Chapelle, S. Lefrant, P. Deniard, R. Leek, and J. E. Fischer, "Large-scale production of single-walled carbon nanotubes by the electric-arc technique," *Nature*, vol. 388, pp. 756–758, August 1997.

[8] S. Iijima and T. Ichihashi, "Single-shell carbon nanotubes of 1-nm diameter," *Nature*, vol. 363, pp. 603–605, June 1993.

[9] P. Nikolaev, M. J. Bronikowski, R. K. Bradley, F. Rohmund, D. T. Colbert, K. Smith, and R. E. Smalley, "Gas-phase catalytic growth of single-walled carbon nanotubes from carbon monoxide," *Chem. Phys. Lett.*, vol. 313, p. 9197, November 1999.

[10] S. Y. Set, H. Yaguchi, Y. Tanaka, , and M. Jablonski, "Laser mode locking using a saturable absorber incorporating carbon nanotubes," *Journal of lightwave Technology*, vol. 22, p. 5156, January 2004.

[11] O. Okhotnikov, A. Grudinin, and M. Pessa, "Ultra-fast bre laser systems based on sesam technology: new horizons and applications," *New J. Phys.*, vol. 6, no. 177, p. 2, 2004.

[12] Y.-W. Song and S. Yamashita, "Carbon nanotube mode lockers with enhanced nonlinearity via evanescent field interaction in d-shaped fibers," *Optics letters*, vol. 32, pp. 148–150, January 2007.

[13] E. Hecht, *Optics*. Addison-Wesley, 4 ed., 2002.

[14] A. W. Snyder and J. D. Love, *Optical Waveguide Theory*. Chapman and Hall, 1983.

[15] G. P. Agrawal, *Nonlinear Fiber Optics*. Elsevier, 4 ed., 2007.

[16] O. Svelto, *Principle of Lasers*. Springer Science+Buisness Media, 4 ed., 1998. Figures used from pages 331 and 333.

[17] L. Råde and B. Westergren, *Mathematics Handbook for Science and Engineering*. Lennart Råde, Bertil Westergren and Studentlitteratur, 5 ed., 2004.

[18] H. A. Haust, "Theory of mode locking with a fast saturable absorber," *J. Appl. Phys.*, vol. 46, pp. 3049–3058, July 1975.

[19] J. W. G. Wilder, L. C. Venema, A. G. Rinzler, R. E. Smalley, and C. Dekker, "Electronic structure of atomically resolved carbon nanotubes," *Nature*, vol. 391, pp. 59–61, January 1998.

[20] S. Yamashita, "A tutorial on nonlinear photonic applications of carbon nanotube and graphene," *Journal of lightwave technology*, vol. 30, pp. 427–447, February 2012.

[21] S. M. Bachilo, M. S. Strano, C. Kittrell, R. H. Hauge, R. E. Smalley, and R. B. Weisman, "Structure-assigned optical spectra of single-walled carbon nanotubes," *Science*, vol. 298, pp. 2361–2366, December 2002.

[22] K. Seger, N. Meiser, S. Y. Choi, B. H. Jung, D. I. Yeom, F. Rotermund, O. Okhotnikov, F. Laurell, and V. Pasiskevicius, "Carbon nanotube mode-locked optically-pumped semiconductor disk laser," *Optics Express*, vol. 21, July 2013.

[23] C. Lu and J. Liu, "Controlling the diameter of carbon nanotubes in chemical vapor deposition method by carbon feeding," *J. Phys. Chem. B*, vol. 110, pp. 20254–20257, August 2006.

[24] Thorlabs, "Single mode fiber with ϕ900 μm hyrtel jacket," November 2013. Available: http://www.thorlabs.de/thorcat/5300/HI1060-100-SpecSheet.pdf.

[25] J. W. Nicholson, R. S. Windeler, and D. J. DiGiovanni, "Optically driven deposition of single-walled carbon-nanotube saturable absorbers on optical fiber end-faces," *Optics Express.*, vol. 15, July 2007.

[26] OneFive, "Origami-10 femtosecond laser," October 2013. Available: http://www.onefive.com/ds/Origami.pdf.

[27] G. P. Agrawal, *Nonlinear Fiber Optics.* Academic Press, 3 ed., 2001. Figures used from pages 9 and 39.

[28] D. Milam and M. J. Weber, "Measurement of nonlinear refractive-index coefficients using time-resolved interferometry: Application to optical materials for high-power neodymium lasers," *J. Appl. Phys.*, vol. 47, pp. 2497–2501, June 1976.

[29] W. B. Cho, J. H. Yim, S. Y. Choi, S. Lee, A. Schmidt, G. Steinmeyer, U. Griebner, V. Petrov, D.-I. Yeom, K. Kimand, and F. Rotermund, "Boosting the nonlinear optical response of carbon nanotube saturable absorbers for broadband mode-locking of bulk lasers," 2010.

[30] N. Meiser, *Novel Technologies for Mode-Locking of Solid-Sate Lasers.* PhD thesis, KTH - Royal Institute of Technology, 2013.